bioRxiv preprint doi: https://doi.org/10.1101/659938; this version posted June 4, 2019. The copyright holder for this preprint (which was not certified by peer review) is the author/funder, who has granted bioRxiv a license to display the preprint in perpetuity. It is made available under aCC-BY-NC-ND 4.0 International license.

1 # Mps1 releases Mad1 from nuclear pores to ensure a robust
2 # mitotic checkpoint and accurate chromosome segregation
3

4 Mariana Osswald[1,2,7], Sofia Cunha-Silva[1,2,7], Jana Goemann[1,2], João Barbosa[1,2], Luis M
5 Santos[3], Pedro Resende[1,2], Tanja Bange[4], Claudio E Sunkel[1,2,5,6] and Carlos Conde[1,2,6]
6
7 [1] i3S, Instituto de Investigação e Inovação em Saúde, Universidade do Porto, Porto, Portugal.
8 [2] IBMC, Instituto de Biologia Molecular e Celular, Universidade do Porto, Porto, Portugal.
9 [3] Faculty of Medicine, University of Geneva, Geneva, Switzerland.
10 [4] Institute for Medical Psychology, Ludwig Maximilian University of Munich, Munich,
11 Germany
12 [5] ICBAS, Departamento de Biologia Molecular, Instituto de Ciências Biomédicas Abel
13 Salazar, Porto, Portugal.
14
15
16
17 [6] Author for correspondence:
18 Carlos Conde (cconde@ibmc.up.pt) ORCID: 0000-0002-4177-8519
19 Rua Alfredo Allen 208,
20 4200-135, Porto, Portugal
21 Tel: +351 220 408 800
22
23 [7] These authors contributed equally to this work
24
25
26
27
28
29
30 **Running Title:** Mps1 at NPCs licenses Mad1 KT recruitment
31

32 **Key words:**
33 Mps1, Megator/Tpr, Mad1, Mitosis, Spindle Assembly Checkpoint, Nuclear pores,
34 Kinetochores

bioRxiv preprint doi: https://doi.org/10.1101/659938; this version posted June 4, 2019. The copyright holder for this preprint (which was not certified by peer review) is the author/funder, who has granted bioRxiv a license to display the preprint in perpetuity. It is made available under aCC-BY-NC-ND 4.0 International license.

35 **ABSTRACT**

36 The strength of the Spindle Assembly Checkpoint (SAC) depends on the amount of the
37 Mad1-C-Mad2 heterotetramer at kinetochores but also on its binding to Megator/Tpr at
38 nuclear pore complexes (NPCs) during interphase. However, the molecular underpinnings
39 controlling the spatiotemporal redistribution of Mad1-C-Mad2 as cells progress into mitosis
40 remain elusive. Here, we show that Mps1-mediated phosphorylation of Megator/Tpr
41 abolishes its interaction with Mad1 *in vitro* and in *Drosophila* cells. Timely activation of
42 Mps1 during prophase triggers Mad1 release from NPCs, which we find to be required for
43 competent kinetochore recruitment of Mad1-C-Mad2 and robust checkpoint response.
44 Importantly, preventing Mad1 binding to Megator/Tpr rescues the fidelity of chromosome
45 segregation and aneuploidy in larval neuroblasts of *Drosophila mps1*-null mutants. Our
46 findings demonstrate that the subcellular localization of Mad1 is stringently coordinated with
47 cell cycle progression by kinetochore-extrinsic activity of Mps1. This ensures that both NPCs
48 in interphase and kinetochores in mitosis can generate anaphase inhibitors to efficiently
49 preserve genomic stability.

50
51
52
53
54
55
56
57
58
59
60
61
62
63
64
65
66
67
68

bioRxiv preprint doi: https://doi.org/10.1101/659938; this version posted June 4, 2019. The copyright holder for this preprint (which was not certified by peer review) is the author/funder, who has granted bioRxiv a license to display the preprint in perpetuity. It is made available under aCC-BY-NC-ND 4.0 International license.

69 **INTRODUCTION**

70 The Spindle Assembly Checkpoint (SAC) safeguards eukaryotic cells against chromosome
71 mis-segregation by restraining the transition to anaphase in the presence of unattached
72 kinetochores. Pivotal to this signalling pathway, is the Mad1-Mad2 heterotetramer that
73 catalyses the structural conversion of soluble open-Mad2 (O-Mad2) into closed-Mad2 (C-
74 Mad2), a conformer that is able to bind the APC/C activator Cdc20 (De Antoni et al., 2005).
75 This represents the rate-limiting step in the assembly of the mitotic checkpoint complex
76 (MCC), a diffusible tetrameric complex that inhibits APC/C-mediated ubiquitination of
77 securin and cyclin B and thereby delays sister chromatid separation and mitotic exit (De
78 Antoni et al., 2005; Simonetta et al., 2009; Faesen et al., 2017). Compelling evidence indicate
79 that the strength of the SAC response is dictated by the amount of Mad1-C-Mad2 present at
80 kinetochores (Collin et al., 2013; Dick and Gerlich, 2013; Hustedt et al., 2014). However, a
81 sustained SAC signalling also requires Mad1-C-Mad2 to associate with nuclear pore
82 complexes (NPCs) during interphase, which is mediated through Mad1 binding to the nuclear
83 basket nucleoporin Megator/Tpr (Scott et al., 2005; Lee et al., 2008; Souza et al., 2009;
84 Lince-Faria et al., 2009; Schweizer et al., 2013; Rodriguez-Bravo et al., 2014). This
85 arrangement regulates Mad1-C-Mad2 proteostasis to ensure that sufficient amount of
86 complexes are produced before mitosis (Schweizer et al., 2013). Moreover, it was proposed
87 that Mad1-C-Mad2 at NPCs also activates O-Mad2 into C-Mad2, hence providing a scaffold
88 for the assembly of pre-mitotic MCC (Rodriguez-Bravo et al., 2014). This is thought to
89 operate as a mitotic timer to support APC/C inhibition during early mitosis until newly
90 formed kinetochores are able to instate efficient SAC activation (Sudakin et al., 2001;
91 Meraldi et al., 2004; Malureanu et al., 2009; Maciejowski et al., 2010; Rodriguez-Bravo et
92 al., 2014; Kim et al., 2018). Notwithstanding its importance for mitotic fidelity, how the
93 subcellular redistribution of Mad1-C-Mad2 is coordinated with cell cycle progression
94 remains elusive. Particularly, whether and how regulatory events at NPCs impact on Mad1-
95 C-Mad2 kinetochore localization has not been established so far. We set out to address these
96 questions in *Drosophila*, where the multi-sequential phosphorylation cascade controlling
97 Mad1 kinetochore localization through the Mps1-Knl1-Bub1 pathway (London et al., 2012;
98 Shepperd et al., 2012; Yamagishi et al., 2012; Primorac et al., 2013; London and Biggins,
99 2014; Vleugel et al., 2015; Mora-Santos et al., 2016; Faesen et al., 2017; Ji et al., 2017; Qian
100 et al., 2017; Zhang et al., 2017; Rodriguez-Rodriguez et al., 2018) is inherently absent
101 (Schittenhelm et al., 2009; Conde et al., 2013). This reduces kinetochore-associated
102 complexity, hence providing a simpler naturally occurring system to uncover the potential

bioRxiv preprint doi: https://doi.org/10.1101/659938; this version posted June 4, 2019. The copyright holder for this preprint (which was not certified by peer review) is the author/funder, who has granted bioRxiv a license to display the preprint in perpetuity. It is made available under aCC-BY-NC-ND 4.0 International license.

103 role of kinetochore-extrinsic mechanisms in Mad1-C-Mad2 subcellular distribution
104 throughout the cell-cycle and their significance for SAC signalling and genomic integrity *in*
105 *vivo*.
106
107 **RESULTS AND DISCUSSION**
108
109 ***Mps1 triggers Mad1 exclusion from nuclear pore complexes during prophase***
110 To investigate the events underlying the subcellular redistribution of Mad1 during mitotic
111 entry we first monitored with high-temporal resolution the dynamics of Mad1 and Megator
112 localization in *Drosophila* S2 cells (Figure 1A,B and S1A,B). Mad1-EGFP signal at the
113 nuclear envelope (NE) begins to fade during early prophase whereas Megator-EGFP intensity
114 persists until tubulin becomes detectable in the nucleus, an early event of nuclear envelope
115 breakdown (NEB). Interestingly, depletion of Mps1 causes a significantly delay in Mad1-
116 EGFP dissociation from the NE with no discernible impact on Megator-EGFP dynamics
117 (Figure 1A,B and S1A,B). The decline in Mad1-EGFP signal intensity at the NE of Mps1-
118 depleted cells entering mitosis overlaps perfectly with the pattern of Megator-EGFP, hinting
119 that in the absence of Mps1 activity, the exclusion of Mad1 from NPCs is restrained by the
120 presence of the nucleoporin (Figure S1A,B). These results support that Mad1 reallocation
121 from NPCs is triggered before NEB onset in an Mps1-dependent manner. Consistently, a
122 phospho-specific antibody recognizing the activating autophosphorylation (T490Ph) of Mps1
123 T-loop (Jelluma et al., 2008; Moura et al., 2017) decorates the NE throughout prophase, thus
124 indicating that Mps1 is active at NPCs during mitotic entry. We then tested whether inducing
125 Mps1 activation in interphase cells prematurely displaces Mad1 from NPCs. As Mps1 is
126 excluded from the nucleus until late G2/early prophase (Zhang et al., 2011; Jia et al., 2015),
127 we promoted its nuclear import by fusing it with the SV40 large T-antigen nuclear
128 localization signal (EGFP-Mps1^{WT}-NLS). Strikingly, overexpression of EGFP-Mps1^{WT}-NLS
129 efficiently elicits nuclear activation of Mps1 (Figure S1C) and clearly decreases Mad1 levels
130 at NPCs of interphase cells (Figure 1D,E). In contrast, Mad1 association with NPCs remains
131 unaltered in interphase S2 cells overexpressing catalytic dead EGFP-Mps1^{KD}-NLS or EGFP-
132 Mps1^{WT} (Figure 1D,E), which albeit active in the cytoplasm, fails to attain close proximity
133 with the nucleoplasmic side of NPCs (Figure S1C). Collectively, these results demonstrate
134 that timely control of Mps1 nuclear import and activation triggers Mad1 dissociation from
135 NPCs during early prophase before NEB onset.
136

bioRxiv preprint doi: https://doi.org/10.1101/659938; this version posted June 4, 2019. The copyright holder for this preprint (which was not certified by peer review) is the author/funder, who has granted bioRxiv a license to display the preprint in perpetuity. It is made available under aCC-BY-NC-ND 4.0 International license.

137 ***Mps1-mediated phosphorylation of Megator disrupts its interaction with Mad1***

138 Since Mad1 localization at NPCs is mediated by Megator (Scott et al., 2005; Lee et al., 2008;
139 Souza et al., 2009; Lince-Faria et al., 2009; Schweizer et al., 2013; Rodriguez-Bravo et al.,
140 2014) we next sought to examine whether Mps1 activity directly affects this interaction. We
141 found that Megator preferentially co-immunoprecipitates with Mad1 when Mps1 is depleted
142 from mitotically-enriched S2 cells lysates (Figure 2A). Moreover, knocking-down the kinase
143 markedly reduced Megator hyperphosphorylation (Figure 2B), which prompt us to examine
144 whether Megator is directly targeted by Mps1. *In vitro* kinase assays and mass-spectrometry
145 analysis using recombinant Mps1 and fragments of Megator N-terminus potentially involved
146 in Mad1 binding (Lee et al., 2008) revealed that GST-Mps1 phosphorylates MBP-
147 Megator$^{1178\text{-}1655}$ on T1259, T1295, T1338 and T1390. These residues are located in a putative
148 coiled-coil region (Figure 2D), which we found to directly interact with Mad1 N-terminus in
149 pull-down assays (Figure 2E,F). Notably, 6xHis-Mad1$^{1\text{-}493}$ failed to bind with the same
150 efficiency to MBP-Megator$^{1178\text{-}1655/WT}$ that had been previously phosphorylated by GST-
151 Mps1 or to a phosphomimetic version where T1259, T1295, T1338 and T1390 are converted
152 to aspartates (MBP-Megator$^{1178\text{-}1655/T4D}$), thus indicating that phosphorylation of these
153 particular residues negatively regulates Mad1 binding to Megator *in vitro* (Figure 2E,F). To
154 monitor Mad1-Megator interaction in mitotic cells, we resorted to light-activated reversible
155 inhibition by assembled trap (LARIAT). With this optogenetic tool, EGFP-tagged proteins
156 are sequestered into complexes formed by a multimeric protein (MP) and a blue light-
157 mediated heterodimerization Cib1-Cry2 module (Figure 2G,H). MP is fused to the
158 cryptochrome-interacting basic helix-loop-helix 1 (Cib1), to which the cryptochrome Cry2 is
159 able to bind when photoactivated (Kennedy et al., 2010; Lee et al., 2014; Osswald et al.,
160 2019). By tagging Cry2 with an anti-GFP nanobody, we were able to induce clustering of
161 wild-type (WT), phosphodefective (T4A) and phosphomimetic (T4D) versions of EGFP-
162 Megator$^{1178\text{-}1655}$ with high spatiotemporal resolution and examine their capacity to recruit
163 Mad1 (Figure 2G,H). Immunofluorescence analysis reveals limited association of Mad1 with
164 clusters of EGFP-Megator$^{1178\text{-}1655/WT}$ present in the cytoplasm of colchicine-treated S2 cells
165 (Figure 2G,I). However, a significant increment in Mad1 recruitment to clustered EGFP-
166 Megator$^{1178\text{-}1655/WT}$ occurs upon depletion of Mps1 and similar levels of Mad1 are observed at
167 clusters of EGFP-Megator$^{1178\text{-}1655/T4A}$ (Figure 2G,I). Importantly, Mad1 fails to associate with
168 clusters of EGFP-Megator$^{1178\text{-}1655/T4D}$, even after Mps1 knock-down (Figure 2G,I).
169 Collectively, these results demonstrate that Mps1-mediated phosphorylation of Megator on
170 T1259, T1395, T1338 and T1390 prevents it from binding to Mad1 during mitosis.

bioRxiv preprint doi: https://doi.org/10.1101/659938; this version posted June 4, 2019. The copyright holder for this preprint (which was not certified by peer review) is the author/funder, who has granted bioRxiv a license to display the preprint in perpetuity. It is made available under aCC-BY-NC-ND 4.0 International license.

171

172 ***Recruitment of Mad1 to unattached kinetochores requires its dissociation from Megator***

173 We then sought to examine the relevance of disengaging Mad1 from Megator in mitosis.
174 With the LARIAT experiment we observed that Mad1 levels at EGFP-Megator$^{1178\text{-}1655}$
175 clusters and its accumulation at unattached kinetochores are inversely correlated (Figure 2G-
176 J). This suggests that retaining Mad1 associated with Megator during mitosis precludes its
177 proper recruitment to kinetochores. To address this further, we generated S2 cell lines stably
178 expressing full length versions of Megator phosphomutants tagged with EGFP and depleted
179 the endogenous nucleoporin with RNAi targeting the transcript UTRs (Figure 3A and 4A,B).
180 Following an induction period of 24 hours, all transgenes are expressed at endogenous levels
181 and localize correctly at the NE of interphase cells (Figure 3B; Figure 4A,B). Expression of
182 Megator^{T4D}-EGFP fails to rescue Mad1 loss from NPCs caused by depletion of the
183 endogenous protein, further confirming that phosphorylation of T1259, T1395, T1338 and
184 T1390 inhibits Megator interaction with Mad1 (Figure 3A-C). Conversely, Megator^{T4A}-EGFP
185 is able to restore Mad1 association with interphase NPCs (Figure 3A-C) but impairs its
186 proper recruitment to unattached kinetochores. Expression of EGFP-Megator^{T4A} in
187 colchicine-treated cells results in a two-fold reduction of kinetochore-associated Mad1 levels
188 when compared to Megator$^{WT\text{-}}$EGFP cells (Figure 3D,E). An antibody that specifically
189 recognizes the closed conformer of Mad2 (Fava et al., 2011) reveals a similar decrease in the
190 amount of C-Mad2 at unattached kinetochores of EGFP-Megator^{T4A} cells (Figure 4C,D). As
191 expected, knocking-down Mps1 abrogates Mad1 and C-Mad2 kinetochore localization in
192 cells expressing Megator$^{WT\text{-}}$EGFP (both reduced to ~20% relative to control Megator$^{WT\text{-}}$
193 EGFP cells, Figure 3D,E and 4C,D). Strikingly, this is ameliorated by precluding Mad1
194 interaction with Megator. Cells expressing Megator^{T4D}-EGFP are still partially competent in
195 recruiting Mad1, and to some extent, C-Mad2 to unattached kinetochores upon depletion of
196 Mps1 kinase (~70% of Mad1 levels and ~50% of C-Mad2 levels relative to control
197 Megator$^{WT\text{-}}$EGFP cells, Figure 3D,E and 4C,D). Collectively, these results strongly suggest
198 that kinetochore recruitment of a significant fraction (~50%) of Mad1-C-Mad2
199 heterotetramers requires the dissociation of Mad1 from Megator driven by Mps1-mediated
200 phosphorylation of the latter.

201

202 ***Dissociation of Mad1 from Megator in mitosis is required for functional SAC signalling***

203 To examine the importance of Mps1-mediated phosphorylation of Megator for SAC
204 signalling, we monitored by live-cell imaging the mitotic progression of Megator

bioRxiv preprint doi: https://doi.org/10.1101/659938; this version posted June 4, 2019. The copyright holder for this preprint (which was not certified by peer review) is the author/funder, who has granted bioRxiv a license to display the preprint in perpetuity. It is made available under aCC-BY-NC-ND 4.0 International license.

205 phosphomutants and assessed their capacity to arrest in mitosis when incubated with spindle
206 poisons (Figure 3F). In asynchronous cultures, Megator^{T4A}-EGFP cells progressed slightly
207 faster from NEB to anaphase onset (~36 min) than cells expressing Megator^{WT}-EGFP (~39
208 min), suggesting that the SAC might be partially compromised in the phosphodefective
209 mutant. In line with SAC proficiency, cells expressing Megator^{WT}-EGFP significantly
210 delayed the transition to anaphase in the presence of colchicine (~640 min) or taxol (~180
211 min). In contrast, Megator^{T4A}-EGFP cells, although able to exhibit some mitotic delay in
212 response to unattached kinetochores (~360 min in colchicine) or decreased microtubules
213 dynamics (~87 min in taxol), failed to maintain this to the same time extent as Megator^{WT}-
214 EGFP cells (Figure 3F). These results indicate that preventing the phosphorylation of
215 Megator on T1259, T1395, T1338 and T1390 results in a weakened SAC function, which
216 correlates with the observed reduction (~50%) in Mad1 and C-Mad2 levels at unattached
217 kinetochores. Thus, we reason that phosphorylation of this patch of threonine residues by
218 Mps1 kinase is required to release Mad1 from Megator to provide the kinetochore with
219 sufficient amount of Mad1-C-Mad2 template that ensures a robust SAC response.
220
221 ***Constitutive phosphorylation of Megator reduces C-Mad2 levels at kinetochores and***
222 ***compromises SAC strength***
223 Mad1 and Mad2 form a highly stable complex *in vitro* (Sironi et al., 2002; De Antoni et al.,
224 2005; Vink et al., 2006) and interact with each other throughout the cell cycle (Chen et al.,
225 1998; Chung and Chen, 2002; Fava et al., 2011; Schweizer et al., 2013). Interestingly,
226 although Megator^{T4D}-EGFP cells can recruit Mad1 to unattached kinetochores, we observe an
227 evident decline in the accumulation of C-Mad2 compared to cells expressing Megator^{WT}-
228 EGFP (Figure 4C,D). This phenotype is highly reminiscent of that observed in cells depleted
229 of Megator (Figure 4F,G and S2D-F), which in mammals has been attributed to increased
230 proteolytic degradation of Mad1 and Mad2 (Schweizer et al., 2013). Although we confirm in
231 *Drosophila* cells a significant reduction in the total levels of Mad1 and Mad2 following
232 Megator depletion (Figure 4A,B and S2D), these are partially rescued to a similar extent
233 regardless the Megator-EGFP transgene expressed (Figure 4A,B). This argues against altered
234 Mad1 and Mad2 proteostasis as the main underlying cause for deficient C-Mad2
235 accumulation at kinetochore of Megator^{T4D}-EGFP cells. Instead, we envisage that
236 Megator/Tpr might function *in vivo* as a scaffold for the assembly of the Mad1-C-Mad2
237 complex before its targeting to kinetochores. Kinetochore loading of C-Mad2 is therefore
238 expected to occur inefficiently if Mad1 fails to bind Megator, as in interphase cells where the

bioRxiv preprint doi: https://doi.org/10.1101/659938; this version posted June 4, 2019. The copyright holder for this preprint (which was not certified by peer review) is the author/funder, who has granted bioRxiv a license to display the preprint in perpetuity. It is made available under aCC-BY-NC-ND 4.0 International license.

239 endogenous nucleoporin is depleted or replaced by the phosphomimetic version of the
240 protein. In line with limited C-Mad2 at kinetochores, cells expressing Megator^{T4D}-EGFP
241 failed to arrest in mitosis in response to colchicine as efficiently as Megator^{WT}-EGFP cells
242 (Figure 4E). This is indicative of a weakened SAC function, which is also observed in
243 parental S2 cells and human cultured cells respectively depleted of Megator (Figure 4H and
244 S2G) or Tpr (Schweizer et al., 2013; Rodriguez-Bravo et al., 2014). Hence, while Mad1
245 dissociation from Megator triggered during mitotic entry efficiently endorses Mad1-C-Mad2
246 to unattached kinetochores, abrogating Mad1-Megator interaction during interphase is
247 detrimental for SAC signalling as it possibly compromises the assembly of Mad1-C-Mad2
248 heterotetramers (Schweizer et al., 2013) and the formation of pre-mitotic MCC (Rodriguez-
249 Bravo et al., 2014).
250
251 ***Precluding Mad1 from binding to Megator rescues chromosome mis-segregation and***
252 ***aneuploidy in neuroblasts and intestinal stem cells depleted of Mps1***
253 The results so far demonstrate that Mps1 controls Mad1 kinetochore recruitment in part by
254 abolishing its interaction with Megator. We next assessed whether this mechanism occurs *in*
255 *vivo* and its relevance for genomic stability. We prevented Mps1 kinetochore localization in
256 *Drosophila* 3rd instar larval neuroblasts and examined their capacity to recruit Mad1 to
257 unattached kinetochores. For that, we resorted to *mps1*-null mutant flies (*ald*^{G4422}) expressing
258 a truncated version of Mps1 that lacks the N-terminus domain (gEGFP-Mps1-C^{term}) required
259 for kinetochore targeting (Althoff et al., 2012; Conde et al., 2013). As expected, Mad1
260 inability to localize at kinetochores of colchicine-treated *ald*^{G4422} neuroblasts was largely
261 rescued by the expression of gEGFP-Mps1-WT (Figure S2A-C). Importantly, neuroblasts
262 expressing the gEGFP-Mps1-C^{term} transgene under control of *mps1* promoter were still able
263 to partially recruit Mad1 to unattached kinetochores, accumulating up to 50% of the levels
264 detected in control *w*^{1118} flies (Figure S2A-C). This confirms *in vivo* a kinetochore-extrinsic
265 role for Mps1 in Mad1 kinetochore localization.
266 Collectively, our results indicate that non-kinetochore Mps1 abolishes the interaction
267 between Megator and Mad1 in mitosis, which would otherwise preclude efficient recruitment
268 of Mad1-C-Mad2 to unattached kinetochores. This rationale is further supported *in vivo* by
269 the observation that RNAi-mediated repression of Megator extensively restores Mad1
270 kinetochore recruitment in a *ald*^{G4422} genetic background (Figure 5A,B). Importantly, this
271 concomitantly rescues the aneuploidy that is caused by loss of Mps1 activity (Figure 5A).
272 Depletion of Megator from *ald*^{G4422} neuroblasts led to a striking decrease in the frequency of

bioRxiv preprint doi: https://doi.org/10.1101/659938; this version posted June 4, 2019. The copyright holder for this preprint (which was not certified by peer review) is the author/funder, who has granted bioRxiv a license to display the preprint in perpetuity. It is made available under aCC-BY-NC-ND 4.0 International license.

273 mitotic figures exhibiting aneuploid karyotypes (~70% in *ald*^{G4422} *vs* ~30% in
274 *ald*^{G4422}+Megator RNAi; Figure 5A). Given the evident recovery in genomic stability, we
275 hypothesized that depletion of Megator improves the fidelity of chromosome segregation in
276 cells devoid of Mps1 activity. To test this, we monitored by live imaging the mitotic
277 progression of unperturbed (no drugs) larval neuroblasts (Figure 5C-E). Consistent with
278 Mps1 and Megator roles in SAC signalling, neuroblasts depleted of either protein progressed
279 faster through mitosis (~5 min), when compared to *w*^{1118} controls (~7.3 min). Interestingly,
280 although *UAS-MegatorRNAi* and *ald*^{G4422} neuroblasts reveal indistinguishable mitotic
281 timings, the frequency of anaphases with lagging chromosomes is dramatically higher in
282 *mps1*-null mutants (Figure 5C-E). Importantly, depletion of Megator significantly restores the
283 accuracy of segregation in *ald*^{G4422} neuroblasts, albeit failing to extend the time from NEB to
284 anaphase onset (Figure 5C-E). A similar defect in SAC function was observed in cultured S2
285 cells co-depleted of Mps1 and Megator. Although proficient in Mad1 kinetochore recruitment
286 (Figure S2E,F), these cells failed to arrest in mitosis when challenged with colchicine (Figure
287 S2G), as would be expected from compromised Mps1-dependent phosphorylation of Mad1,
288 and consequently, from limited C-Mad2-Cdc20 interaction (Faesen et al., 2017; Ji et al.,
289 2017). Hence, in *Drosophila* neuroblasts undergoing unperturbed mitosis, kinetochore-
290 associated Mad1 is able to efficiently safeguard anaphase fidelity and chromosomal euploidy
291 independently of its SAC function. This is in line with previous studies reporting a role for
292 Mad1 in preventing merotely through pathways that are uncoupled from its interaction with
293 Mad2 and SAC signalling (Emre et al., 2011; Akera et al., 2015). We then tested whether a
294 similar improvement in genomic stability also occurs in adult tissues. We have recently
295 shown that inducing aneuploidy in intestinal stem cells (ISCs) through depletion of Mps1
296 results in severe intestinal dysplasia (Resende et al., 2018, Figure S3A). Here, we confirmed
297 an increased proliferation of ISCs and enteroblasts (EBs) following *EsgGAL4*-driven
298 expression of *UAS-Mps1RNAi* (Figure S3B,C). Importantly, we found that co-expression of
299 *UAS-MegatorRNAi* supresses this dysplastic phenotype, thus suggesting a rescue in the levels
300 of aneuploidy in ISCs as observed for larval neuroblasts. Collectively, these results strongly
301 support that Mad1 dissociation from its nuclear pore receptor represents a critical event for
302 efficient kinetochore localization, for the fidelity of chromosome segregation and
303 consequently, for genome stability *in vivo*.
304
305 Our biochemical, cellular and *in vivo* data concur to demonstrate that Mps1 activity at NPCs
306 early in prophase sets the stage to enable appropriate recruitment of Mad1 by

bioRxiv preprint doi: https://doi.org/10.1101/659938; this version posted June 4, 2019. The copyright holder for this preprint (which was not certified by peer review) is the author/funder, who has granted bioRxiv a license to display the preprint in perpetuity. It is made available under aCC-BY-NC-ND 4.0 International license.

307 unattached/prometaphase kinetochores (Figure 5F). Phosphorylation of Megator by Mps1
308 abrogates the nucleoporin interaction with Mad1, which we find to be essential for
309 kinetochore localization of Mad1-C-Mad2 to levels required to sustain robust SAC signalling
310 and accurate chromosome segregation. We also show that dissociation of Mad1 from NPCs is
311 prevented during interphase by nuclear exclusion of Mps1 and decreased phosphorylation of
312 its activating T-loop. This is most likely important to facilitate Mad1-C-Mad2 interaction and
313 the assembly of MCC prior to kinetochore maturation and SAC activation (Rodriguez-Bravo
314 et al., 2014; Kim et al., 2018). Together, these observations establish that a key function of
315 non-kinetochore Mps1 is to coordinate Mad1 subcellular localization with cell cycle
316 progression, so that both nuclear pores in interphase and kinetochores in mitosis generate
317 anaphase inhibitors that preserve genomic stability (Figure S4).
318
319 **MATERIALS AND METHODS**
320 **S2 cell cultures, RNAi-mediated depletion and drug treatments**
321 The *Drosophila* S2-DGRC cell line (#stock6) was acquired from the Drosophila Genomics
322 Resource Center, Indiana University and was not independently authenticated. The cell lines
323 were routinely tested negative for mycoplasma contamination. Cell cultures, RNAi synthesis
324 and RNAi treatment were performed as previously described (Conde et al., 2013). At
325 selected time points, cells were collected and processed for immunofluorescence, time-lapse
326 microscopy, immunoblotting or immunoprecipitation. When required, cells were subjected
327 to several drug treatments before being collected and processed for the desired analysis. To
328 promote microtubule depolymerisation, cells were incubated with 30 µM colchicine (Sigma–
329 Aldrich, St. Louis, MO) for 30 minutes - 24 hours. To decrease microtubule dynamics cells
330 were incubated with 100 nM taxol (Sigma-Aldrich). When required, 20µM MG132
331 (Calbiochem, San Diego, CA) were added to inhibit the proteasome. For experiments in
332 Figure 1D,E and Figure S1C, cells were incubated with 10µM of Leptomycine B (Sigma-
333 Aldrich) for 3 hours to block Crm1-mediated nuclear export.
334
335 **Constructs and S2 cells transfection**
336 Recombinant plasmids pHWG[blast]-Megator^{WT}, pHWG[blast]-Megator^{T4A}, pHWG[blast]-
337 Megator^{T4D}, pHGW[blast]-Megator$^{1187-1655/WT}$, pHGW[blast]-Megator$^{1187-1655/T4A}$,
338 pHGW[blast]-Megator$^{1187-1655/T4D}$ and pHGW[blast]-Mps1^{WT} were generated using the
339 Gateway Cloning System (Invitrogen). Megator, Megator$^{1187-1655}$ or Mps1 cDNAs were
340 amplified by PCR and inserted into modified versions of pENTR-entry vector through

bioRxiv preprint doi: https://doi.org/10.1101/659938; this version posted June 4, 2019. The copyright holder for this preprint (which was not certified by peer review) is the author/funder, who has granted bioRxiv a license to display the preprint in perpetuity. It is made available under aCC-BY-NC-ND 4.0 International license.

341 FastCloning (Li et al., 2011). To generate pENTR-Megator$^{1187\text{-}1655/T4A}$ and pENTR-
342 Megator$^{1187\text{-}1655/T4D}$ codons corresponding to T1259, T1302, T1338 and T1390 of pENTR-
343 Megator$^{1187\text{-}1655}$ were converted either to codons for alanine (A) or aspartate (D) respectively,
344 by several cycles of site-directed mutagenesis with primers harbouring the desired mutations.
345 To generate pENTR-Megator^{T4A} and pENTR-Megator^{T4D}, the fragment corresponding to
346 amino acids 1187-1655 on pENTR-Megator^{WT} was replaced by Megator$^{1187\text{-}1655/T4A}$ or
347 Megator$^{1187\text{-}1655/T4D}$ PCR products, respectively through FastCloning (Li et al., 2011). PCR
348 reactions were performed using Phusion polymerase (New England Biolabs). PCR products
349 were digested with DpnI restriction enzyme (New England Biolabs), used to transform
350 competent bacteria and selected for positives. Subsequently, pENTR-Megator$^{1187\text{-}1655}$
351 constructs and pENTR-Mps1 were recombined with pHGW[blast] (blasticidin^{R}; N-terminal
352 EGFP tag), and pENTR-Megator constructs with pHWG (blasticidin^{R}; C-terminal EGFP tag)
353 using Gateway LR Clonase II (Invitrogen), according to the manufacturer's instructions.
354 pHGW-Mps1^{WT}-NLS was produced by PCR amplification of pHGW-Mps1^{WT} with primers
355 harbouring SV40 large T-antigen nuclear localization signal sequence. pHGW-Mps1^{KD}-NLS
356 was produced by site-directed mutagenesis of pHGW-Mps1^{WT}-NLS with primers harbouring
357 the mutation to convert D478 to A478. PCR reactions were performed with Phusion
358 polymerase, followed by digestion with DpnI restriction enzyme (New England Biolabs). The
359 constructs H2B-mCherry, H2B-GFP, mCherry-α-Tubulin, Mad1-EGFP, pHW-CIB-MP-
360 HRW-CRY2-V_{H}H, and pHGW-aPKC have been previously described (Conde et al., 2013;
361 Moura et al., 2017; Osswald et al., 2019). Plasmids were transfected into S2 cells using
362 Effectene Transfection Reagent (Qiagen), according to the manufacturer´s instructions.
363 Transiently expressing cells were harvested 4-5 days after transfections. Stable cell lines were
364 obtained by selection in medium with 25 μg/mL blasticidin. To induce expression of pHW-
365 CIB-MP-HRW-CRY2-V_{H}H, pHGW[blast] or pHWG[blast] constructs cells were incubated
366 for 30min at 37ºC 24 hours prior to processing. Cells transfected with pHW-CIB-MP-HRW-
367 CRY2-V_{H}H were maintained in the dark until processing.
368
369 **Live cell imaging**
370 Live analysis of mitosis was performed in S2 cell lines and neuroblasts expressing the
371 indicated constructs. S2 cells were plated on glass bottom dishes (MatTek) coated with
372 Concanavalin A (0.25 mg/mL; Sigma-Aldrich). Third-instar larvae brains were dissected in
373 PBS and mounted in PBS between coverslips of different sizes. The preparation was
374 squashed and sealed with Halocarbon oil 700 (Sigma-Aldrich). 4D datasets were collected at

bioRxiv preprint doi: https://doi.org/10.1101/659938; this version posted June 4, 2019. The copyright holder for this preprint (which was not certified by peer review) is the author/funder, who has granted bioRxiv a license to display the preprint in perpetuity. It is made available under aCC-BY-NC-ND 4.0 International license.

375 25°C with a spinning disc confocal system (Revolution; Andor) equipped with an electron
376 multiplying charge-coupled device camera (iXonEM+; Andor) and a CSU-22 unit
377 (Yokogawa) based on an inverted microscope (IX81; Olympus). Two laser lines (488 and
378 561 nm) were used for near-simultaneous excitation of EGFP and mCherry or RFP. The
379 system was driven by iQ software (Andor). Time-lapse imaging of z stacks with 0.8 µm steps
380 for S2 cells and 0.5µm for neuroblasts were collected and image sequence analysis, video
381 assembly and fluorescence intensities quantification performed using ImageJ software.
382 Quantification of Mad1-EGFP and Megator-EGFP levels at the nuclear envelope and
383 mCherry tubulin at the nucleus was performed on single Z stacks from images acquired with
384 fixed exposure settings. Mad1-EGFP and Megator-EGFP intensities at the nuclear envelope
385 were determined for each time point (t), using the following formula:
386

$$\frac{(\mathrm{Bi} - \mathrm{bm} \times \mathrm{Ba}) - (\mathrm{Si} - \mathrm{bm} \times \mathrm{Sa})}{(\mathrm{Ba} - \mathrm{Sa})} \times \frac{\mathrm{Cit}}{\mathrm{Cit0}}$$

387

388 Bi -integrated density of a ROI harbouring the nucleus (including outer nuclear membrane);
389 Ba – area of the ROI harbouring the nucleus; Si – integrated density of a ROI encompassing
390 the nucleoplasm; Sa - area of the ROI harbouring the nucleoplasm; bm- mean intensity a ROI
391 outside the cell (background); Cit - integrated density of a ROI harbouring the cell at time t;
392 Cit0- integrated density of a ROI harbouring the cell on the first frame. mCherry-Tubulin
393 intensities in the nucleus were determined for each time point (t), using the following
394 formula:

$$(\mathrm{Nm} - \mathrm{bm}) \times \frac{\mathrm{Cit}}{\mathrm{Cit0}}$$

395 Nm- mean intensity of a ROI inside the nucleus, bm- mean intensity of the background, Cit-
396 integrated density of a ROI harbouring the cell at time t; Cit0- integrated density of a ROI
397 harbouring the cell on the first frame. The changes in fluorescence intensity over time were
398 plotted as normalized signal relative to the mean signal measured before NEB.
399

400 **Immunofluorescence analysis**

401 For immunofluorescence analysis of S2 cells, 10^5 cells were centrifuged onto slides for 5 min,
402 at 1500 rpm (Cytospin 2, Shandon). For LARIAT experiments, cells were irradiated with
403 blue light for 30 min prior to centrifugation. Afterwards, cells were fixed in 4%
404 paraformaldehyde in PBS for 12min and further extracted for 8min with 0.1% Triton X-100

bioRxiv preprint doi: https://doi.org/10.1101/659938; this version posted June 4, 2019. The copyright holder for this preprint (which was not certified by peer review) is the author/funder, who has granted bioRxiv a license to display the preprint in perpetuity. It is made available under aCC-BY-NC-ND 4.0 International license.

405 in PBS. Alternatively, cells were simultaneously fixed and extracted in 3.7% formadehyde
406 (Sigma), 0.5 % Triton X-100 in PBS for 10min followed by three washing steps of 5 min
407 with PBS-T (PBS with 0,05% Tween20). For immunofluorescence analysis of *Drosophila*
408 neuroblasts, third-instar larval brains were dissected in PBS and incubated with 50μM
409 colchicine for 1.5h. The brains were after fixed in 1.8% formaldehyde (Sigma-Aldrich) and
410 45% glacial acetic acid for 5min, squashed between slide and coverslip and immersed in
411 liquid nitrogen. Subsequently, coverslips were removed, the slides were incubated in cold
412 ethanol for 10 min and washed in PBS with 0.1% Triton X-100. Immunostaining was
413 performed as previously described (Moura et al., 2017). Fixation and immunostaining of
414 intestines from 20 day adult flies were performed as previously described (Resende et al.,
415 2018). Images were collected in a Zeiss Axio Imager microscope (Carl Zeiss, Germany) or in
416 a Leica TCS II scanning confocal microscope (Leica Microsystems). For
417 immunofluorescence quantification, the mean pixel intensity was obtained from raw images
418 acquired with fixed exposure acquisition settings. Fluorescence intensities at the nuclear
419 envelope were obtained from single Z stack projections. The nuclear envelope was defined
420 based on Megator or Megator-EGFP staining, by subtracting a ROI containing the
421 nucleoplasm to a ROI harboring the entire nucleus (outer membrane) after subtraction of
422 background intensities estimated from regions outside the cell. Mad1 fluorescence intensities
423 were determined relative to Megator or Megator-EGFP. Fluorescence intensities of LARIAT-
424 mediated clustered proteins and kinetochore proteins were obtained from maximum projected
425 images. For Mad1 and EGFP-Megator$^{1187\text{-}1655}$, the fluorescence intensities were quantified for
426 individual clusters selected manually by mRFP-Cry2 staining. After subtraction of
427 background intensities estimated from regions inside of the cell with no clusters, the intensity
428 of Mad1 was determined relative to Megator-EGFP signal. For kinetochore proteins the
429 fluorescence intensity was quantified for individual kinetochores selected manually by Mad1,
430 CID or Spc105 staining. The size of the ROI was predefined so that each single kinetochore
431 could fit into. After subtraction of background intensities, estimated from regions outside the
432 cell, the intensity of the proteins was determined relative to cytoplasmic Mad1, CID or
433 Spc105.
434

435 **S2 cell lysates, immunoprecipitation, and western blotting**

436 For *Drosophila* brain lysates, at least 10 third-instar larvae brains were dissected in PBS,
437 transferred to Laemmli Buffer (4% SDS, 10% β-mercaptoetanol, 0.125M Tris-HCl, 20%

bioRxiv preprint doi: https://doi.org/10.1101/659938; this version posted June 4, 2019. The copyright holder for this preprint (which was not certified by peer review) is the author/funder, who has granted bioRxiv a license to display the preprint in perpetuity. It is made available under aCC-BY-NC-ND 4.0 International license.

438 glycerol and 0.004% bromophenol blue) and boiled at 95ºC for 5min. S2 cell lysates for
439 immunoprecipitation and western blot analysis were obtained from non-transfected S2 cells
440 or S2 cells expressing Megator-EGFP transgenes treated with colchicine and MG132 when
441 indicated. For western blot of total S2 cell lysates, 10^6 cells were harvested through
442 centrifugation at 5000rpm for 10min. The resulting pellet was resuspended in Laemmli
443 sample buffer and boiled at 95ºC for 5min.
444 For immunoprecipitation assays, cells were harvested through centrifugation at 5000 rpm for
445 10 min at 4˚C and afterwards washed with 2mL PBS supplemented with 1x protease
446 inhibitors cocktail (Roche, Basel, Switzerland). Cell pellet was resuspended in lysis buffer
447 (150 mM KCl, 75 mM HEPES, pH 7.5, 1.5 mM EGTA, 1.5 mM MgCl2, 15% glycerol, 0.1%
448 NP-40, 1x protease inhibitors cocktail (Roche) and 1x phosphatase inhibitors cocktail 3
449 (Sigma)) before freezing disruption in liquid nitrogen. Cell lysates were then clarified
450 through centrifugation at 10000 rpm for 10 min at 4˚C and concentration determined
451 measuring Absorbance at 280nm in the Nanodrop 1000 (ThermoFisher). Lysates containing
452 800µg of protein in a total of 400µl lysis buffer were pre-cleared by incubation with 15µl of
453 Protein A magnetic beads (New England Biolabs) for 1h at 4ºC under agitation. Pre-cleared
454 extracts were incubated with rabbit anti-Mad1 (1:100) overnight, at 4ºC under agitation.
455 Afterwards, the mixture was incubated with 40µl of Protein A magnetic beads for 1h30 min,
456 at 4ºC with agitation. Magnetic beads were collected and washed 4 times with 500µL of lysis
457 buffer. Magnetic beads were resuspended Laemmli sample buffer and boiled at 95ºC for 5
458 min. To confirm protein hyperphosphorylation status, 50µg of mitotic cell lysates were
459 treated with 400U of λ-phosphatase (New England Biolabs) at 30˚C for 1 hour in a total
460 volume of 50µl PMP phosphatase buffer (50 mM HEPES pH 7.5, 100 mM NaCl, 2 mM
461 DTT, 0.01% Brij 35, 1 mM $MnCl_2$; New England Biolabs).
462 Samples were resolved by SDS-PAGE and transferred to a nitrocellulose membrane, using
463 the iBlot Dry Blotting System (Invitrogen) according to the manufacturer's instructions.
464 Transferred proteins were confirmed by Ponceau staining (0.25% Ponceau S in 40%
465 methanol and 15% acetic acid). The membrane was blocked for 1 hour at room temperature
466 with 5% powder milk prepared in PBST and subsequently incubated with primary antibodies
467 diluted in blocking solution overnight at 4˚C under agitation. Membranes were washed three
468 times for 10min with PSBT and incubated with secondary antibodies (diluted in blocking
469 solution) for 1 hour at room temperature with agitation. Secondary antibodies conjugated to
470 Horseradish peroxidase (Santa Cruz Biotechnology) or VeriBlot for IP Detection Reagent
471 (HRP) (Abcam, ab131366) were used according to the manufacturer´s instructions. Blots

bioRxiv preprint doi: https://doi.org/10.1101/659938; this version posted June 4, 2019. The copyright holder for this preprint (which was not certified by peer review) is the author/funder, who has granted bioRxiv a license to display the preprint in perpetuity. It is made available under aCC-BY-NC-ND 4.0 International license.

472 were developed with ECL Chemiluminescent Detection System (Amersham) according to
473 manufacturer's protocol and detected on X-ray film (Fuji Medical X-Ray Film). When
474 required proteins were resolved in 4-20% Mini-PROTEAN® TGX Precast Gel (BioRad) and
475 transferred to nitrocellulose membrane overnight in 48mM Tris, 39mM glycine, 0.037%
476 SDS, 20% metanol, pH=8.3, at 20V, 4ºC.
477

478 **Production and purification of recombinant proteins**

479 To generate 6xHis-Mad1$^{1-493}$ and 6xHis-BubR1$^{1-358}$ constructs for expression in bacteria,
480 PCR products with the coding sequence were cloned into NdeI/XhoI or SalI/XhoI sites of
481 pET30a (+) vector (Novagen, Darmstadt, Germany), respectively. TOP10 competent cells
482 were transformed and selected for positives. The recombinant construct was used to
483 transform BL21-star competent cells and protein expression induced with 0.05mM IPTG at
484 15ºC, overnight. Cells were harvested and lysed in bacterial lysis buffer (50mM NaH_2PO_4,
485 300mM NaCl, 10mM imidazole, pH=8.0) supplemented with 1mM PMSF (Sigma),
486 0.4mg/ml Lysozyme (Sigma), sonicated and clarified by centrifugation at 4ºC. Recombinant
487 6xHis-Mad1$^{1-493}$, 6xHis-BubR1$^{1-358}$ were purified with Novex Dynabeads (Invitrogen) in
488 bacterial lysis buffer.
489 To generate recombinant MBP-Megator fragments (a.a. 1-402; 403-800; 1187-1655), PCR
490 products harboring the coding sequences for fragments 1-402, 403-800 and 1187-1655 of
491 Megator were cloned into pMal-c2 (New England Biolabs) vector. Megator $^{1187-1655/T4A}$ and
492 Megator $^{1187-1655/T4D}$ were inserted into pMal-c2 vector through FastCloning (Li et al., 2011)
493 using Phusion Polymerase (New England Biolabs). These constructs were used to transform
494 TOP10 competent bacteria and cells were selected for the incorporation of plasmids. The
495 selected recombinant constructs were used to transform BL21-star competent cells and
496 protein expression induced with 0.05 mM IPTG at 15˚C, overnight. Pellets of these cultures
497 were lysed in column buffer (200 mM NaCl, 20 mM Tris-HCl, 1 mM EDTA, 1mM DTT,
498 pH=7.4) supplemented with 1% Triton X100 (Sigma), 1mM PMSF (Sigma), and 0.4 mg/ml
499 of lysozyme (Sigma), sonicated and clarified by centrifugation at 4ºC. Recombinant MBP-
500 Megator fragments were purified with amylose magnetic beads (New England Biolabs) and
501 eluted in Column Buffer supplemented with 10mM Maltose. The purified recombinant
502 proteins (eluted or bound to magnetic beads) were resolved by SDS-PAGE and their relative
503 amounts determined after Coomassie blue staining. Similar amounts of protein were used in
504 the subsequent assays.
505

bioRxiv preprint doi: https://doi.org/10.1101/659938; this version posted June 4, 2019. The copyright holder for this preprint (which was not certified by peer review) is the author/funder, who has granted bioRxiv a license to display the preprint in perpetuity. It is made available under aCC-BY-NC-ND 4.0 International license.

506 ***In vitro* kinase assays, mass spectrometry analysis and pull-down assays**

507 For *in vitro* kinase assays, recombinant fragments of MBP-Megator were incubated with
508 0.05µg HsMps1/TTK (SignalChem, Richmond, Canada) in a total volume of 30µl kinase
509 reaction buffer (5 mM MOPS pH 7.2, 2.5 mM β-glycerol-phosphate, 5 mM MgCl2, 1 mM
510 EGTA, 0.4 mM EDTA, 0.25 mM DTT, 100 µM ATP and supplemented with 1× phosphatase
511 inhibitors cocktail 3 (Roche). Reactions were carried out at 30ºC for 30 min, and analysed by
512 autoradiography, subjected to mass spectrometry analysis or used in pull-down assays. For
513 detection of ^{32}P incorporation, the kinase reaction buffer was supplemented with 10 μ Ci [γ -
514 ^{32}P] ATP [3000Ci/mmol, 10mCi/mL] and the reaction was stopped by addition of Laemmli
515 sample buffer, boiled for 5min at 95ºC and resolved by SDS-PAGE. After drying at 80ºC
516 under vacuum, the gel was exposed to X-ray films (Fuji Medical X-Ray Film). For
517 identification of phosphorylated residues, the reaction was stopped by addition of 6M Urea
518 and subsequently analyzed by liquid chromatography coupled with mass spectrometry.
519 Samples were digested with LysC/Trypsin and/or GluC and prepared for LC-MS/MS analysis
520 as previously described (Rappsilber et al., 2007). Peptides (100ng) were separated on a
521 Thermo ScientificTM EASY-nLC 1000 HPLC system (Thermo Fisher ScientificTM) for
522 1hour from 5-60% acetonitrile with 0.1% fromic acid and directly sprayed via a nano-
523 electrospray source in a quadrupole Orbitrap mass spectrometer (Q ExactiveTM, Thermo
524 Fisher ScientificTM) (Michalski et al., 2011). The Q ExactiveTM was operated in data-
525 dependent mode acquiring one survey scan and subsequently ten MS/MS scans (Olsen et al.,
526 2007). Resulting raw files were processed with the MaxQuant software (version 1.5.2.18)
527 using a reduced database containing only the proteins of interest and giving phosphorylation
528 on serine, threonine and tyrosine as variable modification (Cox and Mann, 2008). A false
529 discovery rate cut off of 1% was applied at the peptide and protein levels and the
530 phosphorylation site decoy fraction.

531 For pull-down assays, 6xHis-Mad1$^{1\text{-}493}$ or 6xHis-BubR1$^{1\text{-}358}$ bound to Novex Dynabeads
532 (Invitrogen) were incubated with the MPB-Megator$^{1187\text{-}1655}$ constructs in a final volume of
533 50µL column buffer (250 mM NaCl, 20 mM Tris-HCl pH 7.4, 1 mM EDTA, 1 mM DTT,
534 0.05% Tween20 (Sigma) 1x protease inhibitors cocktail (Roche) and 1x phosphatase
535 inhibitors cocktail 3 (Sigma-Aldrich) for 1h30min at room temperature with agitation. The
536 magnetic beads (with bound protein) were collected and washed 3 times with 500µL column
537 buffer, resuspended in Laemmli sample buffer and boiled at 95ºC for 5 min. After removal of

bioRxiv preprint doi: https://doi.org/10.1101/659938; this version posted June 4, 2019. The copyright holder for this preprint (which was not certified by peer review) is the author/funder, who has granted bioRxiv a license to display the preprint in perpetuity. It is made available under aCC-BY-NC-ND 4.0 International license.

538 the magnetic beads, samples were resolved by SDS-PAGE and probed for proteins of interest
539 through western blotting.
540

541 **Antibodies**

542 The following primary antibodies were used for immunofluorescence studies: rat anti-CID
543 (Rat4) used at 1:250, rabbit anti-phosphorylated Thr676-Mps1 (T676) (a gift from Geert
544 Kops, (Jelluma et al., 2008) used at 1:2000, chicken anti-GFP (Abcam, ab 13970) used at
545 1:2000 for S2 cells and 1:1000 in neuroblasts, mouse anti-Megator (gift from Jørgen
546 Johansen and Kristen Johansen, Qi et al., 2004, RRID:AB_2721935), used at 1:20, rabbit
547 anti-Mad1 (Rb1, Conde et al., 2013) used at 1:2500 for S2 cells and 1:1000 for neuroblasts,
548 mouse anti-C-Mad2 (Sigma), used at 1:50 for S2 cells and 1:25 for neuroblasts, rat anti-
549 Spc105 used at 1:250, guinea pig anti-Mps1 (Gp15) (a gift from Scott Hawley,
550 RRID:AB_2567774) used at 1:250, rabbit anti-phosphorylated ser10-Histone H3 (p-H3)
551 (Milipore, Billerica, MA, RRID:AB_565299) used at 1:5000, rabbit anti-GFP (Molecular
552 Probes) used at 1:5000 for *Drosophila* intestines. The following primary antibodies were
553 used for western blotting studies: mouse anti-α-tubulin DM1A (Sigma-Aldrich,
554 RRID:AB_477593) used at 1:10000; rabbit anti-Cyclin B (gift from C. Lehner) used at
555 1:10000, guinea pig anti-Mps1 (Gp15) (a gift from Scott Hawley, RRID:AB_2567774) used
556 at 1:5000; mouse anti-Megator (gift from Jørgen Johansen and Kristen Johansen, Qi et al.,
557 2004, RRID:AB_2721935) used at 1:100, rabbit anti-Mad1 (Rb1,(Conde et al., 2013) used at
558 1:2000, rabbit anti-Mad2 (Rb 1223) used at 1:100, mouse anti-MBP (New England
559 Biolabs, RRID:AB_ 1559738), used at 1:5000; mouse anti His Tag (Milipore, 05-949) used
560 at 1:2500.
561

562 **Fly stocks**

563 All fly stocks were obtained from Bloomington Stock Center (Indiana, USA), unless stated
564 otherwise. The mps1 mutant allele ald^{G4422} has been described before (Conde et al., 2013).
565 *Insc-GAL4* was used to drive the expression of *UAS-MegatorRNAi* and *UAS-Mad1RNAi* in
566 neuroblasts from third-instar larvae brains. *EsgGAL4* was used to drive expression of *UAS-*
567 *MegatorRNAi* and *UAS-Mps1RNAi* in ISCs and EBs from intestines of adult flies, as
568 previously described (Resende et al., 2018). w^{1118} was used as wild-type control. Fly stocks
569 harboring gEGFP-MPS1^{WT} and gEGFP-MPS1$^{325-630}$ under control of Mps1 cis-regulatory
570 region were kindly provided by Christian Lehner (Althoff et al., 2012).
571

bioRxiv preprint doi: https://doi.org/10.1101/659938; this version posted June 4, 2019. The copyright holder for this preprint (which was not certified by peer review) is the author/funder, who has granted bioRxiv a license to display the preprint in perpetuity. It is made available under aCC-BY-NC-ND 4.0 International license.

572 **Statistical analysis**

573 All statistical analysis was performed with GraphPad Prism V7.0f (Graph- Pad Software,
574 Inc.).

575

576 **ACKNOWLEDGEMENTS**

577 We thank Geert Kops (Hubrecht Institute, The Netherlands) for the phospho-specific Mps1
578 antibody, Thomas Maresca (University of Massachusetts Amherst, USA) for the Mad1-EGFP
579 construct, Christian Lehner (University of Zurich, Switzerland) for the gEGFP-Mps1-WT
580 and gEGFP-Mps1-C^{term} fly stocks, Eurico Morais-de-Sá (i3S/IBMC, Portugal) for sharing
581 unpublished LARIAT constructs, Helder Maiato (i3S/IBMC, Portugal) for the Megator
582 cDNA and Jørgen Johansen and Kristen Johansen (Iowa State University, USA) for the
583 Megator antibody. We thank Ana Pinto, Nelson Leça and Margarida Moura (i3S/IBMC,
584 Portugal) for technical help and critical reading of the manuscript.

585 This article is a result of the project Norte-01-0145-FEDER-000029 - Advancing Cancer
586 Research: From basic knowledge to application, supported by Norte Portugal Regional
587 Operational Programme (NORTE 2020), under the PORTUGAL 2020 Partnership
588 Agreement, through the European Regional Development Fund (FEDER). MO is supported
589 by a fellowship from the GABBA PhD program from the University of Porto,
590 PD/BD/105746/2014. SC-S is supported by the FCT PhD fellowship
591 SFRH/BD/136527/2018). JB is supported by an FCT PhD grant SFRH/BD/87871/2012. CC
592 is supported by an FCT investigator position and funding (IF/01755/2014).

593

594 The authors declare no competing financial interests

595

596 **AUTHOR CONTRIBUTIONS**

597 Mariana Osswald and Sofia Cunha-Silva performed most of the experiments with
598 contributions from Jana Goemann, Luis M Santos and Carlos Conde. João Barbosa
599 performed the live-imaging experiments with *Drosophila* neuroblasts. Pedro Resende
600 performed the immunofluorescence analysis of *Drosophila* intestines. Tanja Bange
601 performed the mass-spectrometry analysis of *in vitro* kinase assays. Mariana Osswald, Sofia
602 Cunha-Silva, Claudio E Sunkel and Carlos Conde analysed the data. Mariana Osswald and
603 Carlos Conde conceived the project. Carlos Conde designed the experiments, wrote the
604 manuscript and coordinated the project.

605

bioRxiv preprint doi: https://doi.org/10.1101/659938; this version posted June 4, 2019. The copyright holder for this preprint (which was not certified by peer review) is the author/funder, who has granted bioRxiv a license to display the preprint in perpetuity. It is made available under aCC-BY-NC-ND 4.0 International license.

606 **References:**

607 Akera, T., Y. Goto, M. Sato, M. Yamamoto, and Y. Watanabe. 2015. Mad1 promotes
608 chromosome congression by anchoring a kinesin motor to the kinetochore. *Nat. Cell*
609 *Biol.* 17:1124–1133. doi:10.1038/ncb3219.
610 Althoff, F., R.E. Karess, and C.F. Lehner. 2012. Spindle checkpoint-independent inhibition
611 of mitotic chromosome segregation by *Drosophila* Mps1. *Mol. Biol. Cell*. 23:2275–
612 2291. doi:10.1091/mbc.e12-02-0117.
613 De Antoni, A., C.G. Pearson, D. Cimini, J.C. Canman, V. Sala, L. Nezi, M. Mapelli, L.
614 Sironi, M. Faretta, and A. Musacchio. 2005. The Mad1/Mad2 complex as a template for
615 Mad2 activation in the spindle assembly checkpoint. *Curr. Biol.* 15:214–225.
616 doi:10.1016/j.
617 Chen, R.H., A. Shevchenko, M. Mann, and A.W. Murray. 1998. Spindle checkpoint protein
618 Xmad1 recruits Xmad2 to unattached kinetochores. *J. Cell Biol.* 143:283–295.
619 doi:10.1083/jcb.143.2.283.
620 Chung, E., and R.-H. Chen. 2002. Spindle checkpoint requires Mad1-bound and Mad1-free
621 Mad2. *Mol. Biol. Cell*. 13:1501–1511. doi:10.1091/mbc.02.
622 Collin, P., O. Nashchekina, R. Walker, and J. Pines. 2013. The spindle assembly checkpoint
623 works like a rheostat rather than a toggle switch. *Nat. Cell Biol.* 15:1378–1385.
624 doi:10.1038/ncb2855.
625 Conde, C., M. Osswald, J. Barbosa, T. Moutinho-Santos, D. Pinheiro, S. Guimarães, I.
626 Matos, H. Maiato, and C.E. Sunkel. 2013. *Drosophila* Polo regulates the spindle
627 assembly checkpoint through Mps1-dependent BubR1 phosphorylation. *EMBO J.*
628 32:1761–77. doi:10.1038/emboj.2013.109.
629 Cox, J., and M. Mann. 2008. MaxQuant enables high peptide identification rates,
630 individualized p.p.b.-range mass accuracies and proteome-wide protein quantification.
631 *Nat. Biotechnol.* 26:1367–72. doi:10.1038/nbt.1511.
632 Dick, A.E., and D.W. Gerlich. 2013. Kinetic framework of spindle assembly checkpoint
633 signalling. *Nat. Cell Biol.* 15:1370–1377. doi:10.1038/ncb2842.
634 Emre, D., R. Terracol, A. Poncet, Z. Rahmani, and R.E. Karess. 2011. A mitotic role for
635 Mad1 beyond the spindle checkpoint. *J. Cell Sci.* 124:1664–1671.
636 doi:10.1242/jcs.081216.
637 Faesen, A.C., M. Thanasoula, S. Maffini, C. Breit, F. Müller, S. Van Gerwen, T. Bange, and
638 A. Musacchio. 2017. Basis of catalytic assembly of the mitotic checkpoint complex.
639 *Nature*. 542:498–502. doi:10.1038/nature21384.
640 Fava, L.L., M. Kaulich, E.A. Nigg, and A. Santamaria. 2011. Probing the in vivo function of
641 Mad1:C-Mad2 in the spindle assembly checkpoint. *EMBO J.* 30:3322–3336.
642 doi:10.1038/emboj.2011.239.
643 Hustedt, N., M. Langegger, N. Schmidt, S. Heinrich, H. Windecker, K. Sewart, and S. Hauf.
644 2014. Mad1 contribution to spindle assembly checkpoint signalling goes beyond
645 presenting Mad2 at kinetochores. *EMBO Rep.* 15:291–298.
646 doi:10.1002/embr.201338114.
647 Jelluma, N., A.B. Brenkman, I. McLeod, J.R. Yates, D.W. Cleveland, R.H. Medema, and
648 G.J.P.L. Kops. 2008. Chromosomal instability by inefficient Mps1 auto-activation due
649 to a weakened mitotic checkpoint and lagging chromosomes. *PLoS One*. 3:e2415.
650 doi:10.1371/journal.pone.0002415.
651 Ji, Z., H. Gao, L. Jia, B. Li, and H. Yu. 2017. A sequential multi-target Mps1
652 phosphorylation cascade promotes spindle checkpoint signaling. *Elife*. 6:1–23.
653 doi:10.7554/eLife.22513.
654 Jia, H., X. Zhang, W. Wang, Y. Bai, Y. Ling, C. Cao, R.Z. Ma, H. Zhong, X. Wang, and Q.
655 Xu. 2015. A putative N-terminal nuclear export sequence is sufficient for Mps1 nuclear

bioRxiv preprint doi: https://doi.org/10.1101/659938; this version posted June 4, 2019. The copyright holder for this preprint (which was not certified by peer review) is the author/funder, who has granted bioRxiv a license to display the preprint in perpetuity. It is made available under aCC-BY-NC-ND 4.0 International license.

656 exclusion during interphase. *BMC Cell Biol.* 16:1–8. doi:10.1186/s12860-015-0048-6.
657 Kennedy, M.J., R.M. Hughes, L.A. Peteya, J.W. Schwartz, M.D. Ehlers, and C.L. Tucker.
658 2010. Rapid blue-light–mediated induction of protein interactions in living cells. *Nat.*
659 *Methods*. 7:973.
660 Kim, D.H., J.S. Han, P. Ly, Q. Ye, M.A. McMahon, K. Myung, K.D. Corbett, and D.W.
661 Cleveland. 2018. TRIP13 and APC15 drive mitotic exit by turnover of interphase- and
662 unattached kinetochore-produced MCC. *Nat. Commun.* 9:4354. doi:10.1038/s41467-
663 018-06774-1.
664 Lee, S., H. Park, T. Kyung, N.Y. Kim, S. Kim, J. Kim, and W. Do Heo. 2014. Reversible
665 protein inactivation by optogenetic trapping in cells. *Nat. Methods*. 1408:363–376.
666 doi:10.1007/978-1-4939-3512-3_25.
667 Lee, S.H., H. Sterling, A. Burlingame, and F. McCormick. 2008. Tpr directly binds to Mad1
668 and Mad2 and is important for the Mad1-Mad2-mediated mitotic spindle checkpoint.
669 *Genes Dev.* 22:2926–2931. doi:10.1101/gad.1677208.
670 Li, C., A. Wen, B. Shen, J. Lu, Y. Huang, and Y. Chang. 2011. FastCloning: A highly
671 simplified, purification-free, sequence- and ligation-independent PCR cloning method.
672 *BMC Biotechnol.* 11:92. doi:10.1186/1472-6750-11-92.
673 Lince-Faria, M., S. Maffini, B. Orr, Y. Ding, C. Florindo, C.E. Sunkel, Á. Tavares, J.
674 Johansen, K.M. Johansen, and H. Maiato. 2009. Spatiotemporal control of mitosis by the
675 conserved spindle matrix protein megator. *J. Cell Biol.* 184:647–657.
676 doi:10.1083/jcb.200811012.
677 London, N., and S. Biggins. 2014. Mad1 kinetochore recruitment by Mps1-mediated
678 phosphorylation of Bub1 signals the spindle checkpoint. *Genes Dev.* 28:140–52.
679 doi:10.1101/gad.233700.113.
680 London, N., S. Ceto, J.A. Ranish, and S. Biggins. 2012. Phosphoregulation of Spc105 by
681 Mps1 and PP1 regulates Bub1 localization to kinetochores. *Curr. Biol.* 22:900–906.
682 doi:10.1016/j.cub.2012.03.052.
683 Maciejowski, J., K.A. George, M.E. Terret, C. Zhang, K.M. Shokat, and P. V. Jallepalli.
684 2010. Mps1 directs the assembly of Cdc20 inhibitory complexes during interphase and
685 mitosis to control M phase timing and spindle checkpoint signaling. *J. Cell Biol.*
686 190:89–100. doi:10.1083/jcb.201001050.
687 Malureanu, L.A., K.B. Jeganathan, M. Hamada, L. Wasilewski, J. Davenport, and J.M. van
688 Deursen. 2009. BubR1 N Terminus Acts as a Soluble Inhibitor of Cyclin B Degradation
689 by APC/CCdc20 in Interphase. *Dev. Cell*. 16:118–131.
690 doi:10.1016/j.devcel.2008.11.004.
691 Meraldi, P., V.M. Draviam, and P.K. Sorger. 2004. Timing and checkpoints in the regulation
692 of mitotic progression. *Dev. Cell*. 7:45–60. doi:10.1016/j.devcel.2004.06.006.
693 Michalski, A., E. Damoc, J.-P. Hauschild, O. Lange, A. Wieghaus, A. Makarov, N. Nagaraj,
694 J. Cox, M. Mann, and S. Horning. 2011. Mass spectrometry-based proteomics using Q
695 Exactive, a high-performance benchtop quadrupole Orbitrap mass spectrometer. *Mol.*
696 *Cell. Proteomics*. 10:M111.011015. doi:10.1074/mcp.M111.011015.
697 Mora-Santos, M. del M., A. Hervas-Aguilar, K. Sewart, T.C. Lancaster, J.C. Meadows, and
698 J.B.A. Millar. 2016. Bub3-Bub1 Binding to Spc7/KNL1 Toggles the Spindle
699 Checkpoint Switch by Licensing the Interaction of Bub1 with Mad1-Mad2. *Curr. Biol.*
700 26:2642–2650. doi:10.1016/j.cub.2016.07.040.
701 Moura, M., M. Osswald, N. Leça, J. Barbosa, A.J. Pereira, H. Maiato, C.E. Sunkel, and C.
702 Conde. 2017. Protein phosphatase 1 inactivates Mps1 to ensure efficient spindle
703 assembly checkpoint silencing. *Elife*. 6:1–29. doi:10.7554/eLife.25366.
704 Olsen, J. V., B. Macek, O. Lange, A. Makarov, S. Horning, and M. Mann. 2007. Higher-
705 energy C-trap dissociation for peptide modification analysis. *Nat. Methods*. 4:709–712.

bioRxiv preprint doi: https://doi.org/10.1101/659938; this version posted June 4, 2019. The copyright holder for this preprint (which was not certified by peer review) is the author/funder, who has granted bioRxiv a license to display the preprint in perpetuity. It is made available under aCC-BY-NC-ND 4.0 International license.

706 doi:10.1038/nmeth1060.
707 Osswald, M., A.F. Santos, and E. Morais-de-Sá. 2019. Light-Induced Protein Clustering for
708 Optogenetic Interference and Protein Interaction Analysis in Drosophila S2 Cells.
709 *Biomolecules*. 9:61. doi:10.3390/biom9020061.
710 Primorac, I., J.R. Weir, E. Chiroli, F. Gross, I. Hoffmann, S. van Gerwen, A. Ciliberto, and
711 A. Musacchio. 2013. Bub3 reads phosphorylated MELT repeats to promote spindle
712 assembly checkpoint signaling. *Elife*. 2013:1–20. doi:10.7554/eLife.01030.
713 Qi, H., U. Rath, D. Wang, Y.-Z. Xu, Y. Ding, W. Zhang, M.J. Blacketer, M.R. Paddy, J.
714 Girton, J. Johansen, and K.M. Johansen. 2004. Megator, an essential coiled-coil protein
715 that localizes to the putative spindle matrix during mitosis in *Drosophila*. *Mol. Biol.*
716 *Cell*. 15:4854–4865. doi:10.1091/mbc.E04.
717 Qian, J., M.A. García-Gimeno, M. Beullens, M.G. Manzione, G. Van der Hoeven, J.C. Igual,
718 M. Heredia, P. Sanz, L. Gelens, and M. Bollen. 2017. An attachment-independent
719 biochemical timer of the spindle assembly checkpoint. *Mol. Cell*. 68:715–730.
720 doi:10.1016/j.molcel.2017.10.011.
721 Rappsilber, J., M. Mann, and Y. Ishihama. 2007. Protocol for micro-purification, enrichment,
722 pre-fractionation and storage of peptides for proteomics using StageTips. *Nat. Protoc.*
723 2:1896–1906. doi:10.1038/nprot.2007.261.
724 Resende, L.P., A. Monteiro, R. Brás, T. Lopes, and C.E. Sunkel. 2018. Aneuploidy in
725 intestinal stem cells promotes gut dysplasia in *Drosophila*. *J. Cell Biol.* 217:3930–3946.
726 doi:10.1083/jcb.201804205.
727 Rodriguez-Bravo, V., J. Maciejowski, J. Corona, H. kon K. Buch, P. Collin, M.T. Kanemaki,
728 J. V Shah, and P. V Jallepalli. 2014. Nuclear pores protect genome integrity by
729 assembling a premitotic and Mad1-dependent anaphase inhibitor. *Cell*. 156:1017–1031.
730 doi:10.1016/j.cell.2014.01.010.
731 Rodriguez-Rodriguez, J.A., C. Lewis, K.L. McKinley, V. Sikirzhytski, J. Corona, J.
732 Maciejowski, A. Khodjakov, I.M. Cheeseman, and P. V. Jallepalli. 2018. Distinct roles
733 of RZZ and Bub1-KNL1 in mitotic checkpoint signaling and kinetochore expansion.
734 *Curr. Biol.* 28:3422–3429.e5. doi:10.1016/j.cub.2018.10.006.
735 Schittenhelm, R.B., R. Chaleckis, and C.F. Lehner. 2009. Intrakinetochore localization and
736 essential functional domains of *Drosophila* Spc105. *EMBO J.* 28:2374–2386.
737 doi:10.1038/emboj.2009.188.
738 Schweizer, N., C. Ferrás, D.M. Kern, E. Logarinho, I.M. Cheeseman, and H. Maiato. 2013.
739 Spindle assembly checkpoint robustness requires Tpr-mediated regulation of
740 Mad1/Mad2 proteostasis. *J. Cell Biol.* 203:883–893. doi:10.1083/jcb.201309076.
741 Scott, R.J., C.P. Lusk, D.J. Dilworth, J.D. Aitchison, and R.W. Wozniak. 2005. Interactions
742 between Mad1p and the nuclear transport machinery in the east S*accharomyces*
743 *cerevisiae*. *Mol. Biol. Cell*. 16:4362–4374. doi:10.1091/mbc.E05.
744 Shepperd, L.A., J.C. Meadows, A.M. Sochaj, T.C. Lancaster, J. Zou, G.J. Buttrick, J.
745 Rappsilber, K.G. Hardwick, and J.B.A. Millar. 2012. Phosphodependent recruitment of
746 Bub1 and Bub3 to Spc7/KNL1 by Mph1 kinase maintains the spindle checkpoint. *Curr.*
747 *Biol.* 22:891–899. doi:10.1016/j.cub.2012.03.051.
748 Simonetta, M., R. Manzoni, R. Mosca, M. Mapelli, L. Massimiliano, M. Vink, B. Novak, A.
749 Musacchio, and A. Ciliberto. 2009. The influence of catalysis on Mad2 activation
750 dynamics. *PLoS Biol.* 7. doi:10.1371/journal.pbio.1000010.
751 Sironi, L., M. Mapelli, S. Knapp, A. DeAntoni, K.-T. Jeang, and A. Musacchio. 2002. The
752 Mad1-Mad2 complex: implications of a "safety belt" binding mechanism for the spindle
753 checkpoint. *embo J.* 21:2496–2506. doi:10.1107/s0108767302093947.
754 Souza, C.P. De, S.B. Hashmi, T. Nayak, B. Oakley, and S.A. Osmani. 2009. Mlp1 acts as a
755 mitotic scaffold to spatially regulate spindle assembly checkpoint proteins in *Aspergillus*

bioRxiv preprint doi: https://doi.org/10.1101/659938; this version posted June 4, 2019. The copyright holder for this preprint (which was not certified by peer review) is the author/funder, who has granted bioRxiv a license to display the preprint in perpetuity. It is made available under aCC-BY-NC-ND 4.0 International license.

756 *nidulans*. *Mol. Biol. Cell*. 20:2146–2159. doi:10.1091/mbc.E08.
757 Sudakin, V., G.K.T. Chan, and T.J. Yen. 2001. Checkpoint inhibition of the APC/C in HeLa
758 cells is mediated by a complex of BUBR1, BUB3, CDC20, and MAD2. *J. Cell Biol.*
759 154:925–936. doi:10.1083/jcb.200102093.
760 Vink, M., M. Simonetta, P. Transidico, K. Ferrari, M. Mapelli, A. De Antoni, L.
761 Massimiliano, A. Ciliberto, M. Faretta, E.D. Salmon, and A. Musacchio. 2006. In vitro
762 FRAP identifies the minimal requirements for Mad2 kinetochore dynamics. *Curr. Biol.*
763 16:755–766. doi:10.1016/j.cub.2006.03.057.
764 Vleugel, M., M. Omerzu, V. Groenewold, M.A. Hadders, S.M.A. Lens, and G.J.P.L. Kops.
765 2015. Sequential multisite phospho-regulation of KNL1-BUB3 interfaces at mitotic
766 kinetochores. *Mol. Cell*. 57:824–835. doi:10.1016/j.molcel.2014.12.036.
767 Yamagishi, Y., C.-H. Yang, Y. Tanno, and Y. Watanabe. 2012. MPS1/Mph1 phosphorylates
768 the kinetochore protein KNL1/Spc7 to recruit SAC components. *Nat. Cell Biol.* 14:746–
769 752. doi:10.1038/ncb2515.
770 Zhang, G., T. Kruse, B. López-Méndez, K.B. Sylvestersen, D.H. Garvanska, S. Schopper,
771 M.L. Nielsen, and J. Nilsson. 2017. Bub1 positions Mad1 close to KNL1 MELT repeats
772 to promote checkpoint signalling. *Nat. Commun.* 8:15822. doi:10.1038/ncomms15822.
773 Zhang, X., Q. Yin, Y. Ling, Y. Zhang, R. Ma, Q. Ma, C. Cao, H. Zhong, X. Liu, and Q. Xu.
774 2011. Two LXXLL motifs in the N terminus of Mps1 are required for Mps1 nuclear
775 import during G 2 /M transition and sustained spindle checkpoint responses. *Cell Cycle*.
776 10:2742–2750. doi:10.4161/cc.10.16.15927.
777
778
779
780
781
782
783
784
785
786
787
788
789
790
791
792
793
794
795
796

bioRxiv preprint doi: https://doi.org/10.1101/659938; this version posted June 4, 2019. The copyright holder for this preprint (which was not certified by peer review) is the author/funder, who has granted bioRxiv a license to display the preprint in perpetuity. It is made available under aCC-BY-NC-ND 4.0 International license.

797
798
799
800 **FIGURE LEGENDS**

801 **Figure 1: Msp1 promotes the dissociation of Mad1 from nuclear pore complexes during**
802 **prophase.** (A,B) Representative mitotic progression (A) and quantification (B) of Mad1-
803 EGFP or Megator-EGFP levels at nuclear envelope (NE) and of mCherry-Tubulin levels in
804 the nucleus of control and Mps1-depleted *Drosophila* S2 cells . Mitotic progression was
805 monitored through time-lapse microscopy. Time 0s indicates nuclear envelope breakdown
806 (NEB) and was defined as the moment mCherry-Tubulin signal becomes detectable in the
807 nucleus. Mad1-EGFP ($N \geq 7$ cells), Megator-EGFP ($N \geq 6$ cells) and mCherry-Tubulin
808 fluorescence intensities were normalized to the mean value before NEB. (C) Representative
809 immunofluorescence images of Mps1^{T490Ph} localization pattern in interphase and prophase S2
810 cells. (D, E) Representative immunofluorescence images (D) and quantifications (E) of Mad1
811 levels at the nuclear envelope of interphase control S2 cells and interphase S2 cells
812 expressing EGFP-Mps1^{WT}, EGFP-Mps1^{WT}-NLS or EGFP-Mps1^{KD}-NLS. The insets display
813 magnifications of the outlined regions. Mad1 fluorescence intensities at the nuclear envelope
814 were determined relative to Megator signal ($N \geq 21$ cells for each condition). Data
815 information: in (B) data is presented as mean ± SD, in (E) data is presented as median with
816 the interquartile range. Asterisks indicate that differences between mean ranks are
817 statistically significant, **$p<0.005$ (Kruskal-Wallis, Dunn's multiple comparison test). Scale
818 bars: 5µm.
819

820 **Figure 2: Msp1-mediated phosphorylation of Megator disrupts its interaction with**
821 **Mad1.** (A) Immunoprecipitates (IP) of Mad1 from lysates of asynchronous (-colchicine) and
822 mitotically-enriched (+colchicine) S2 cultures incubated in the presence or absence of Mps1
823 RNAi for 120 hours. Colchicine (30µM) was incubated for 10 hours and MG132 (20µM) was
824 added 4 hours prior to cell lysis. Mad1 IPs and corresponding inputs were blotted for the
825 indicated proteins. (B) Western blot analysis of Megator hyperphosphorylation in cell lysates
826 from the same experimental conditions as in (A). To validate the slower migrating band as an
827 hyperphosphorylated form of Megator, the lysate of control colchicine-incubated cells was
828 treated with λ-phosphatase (λPP) for 1 hour. (C) *In vitro* kinase assay with the indicated
829 recombinant fragments of MBP-Megator and GST-Mps1 in the presence of [γ-^{32}P]ATP for

bioRxiv preprint doi: https://doi.org/10.1101/659938; this version posted June 4, 2019. The copyright holder for this preprint (which was not certified by peer review) is the author/funder, who has granted bioRxiv a license to display the preprint in perpetuity. It is made available under aCC-BY-NC-ND 4.0 International license.

830 30 min. Phosphorylation was detected by autoradiography and protein levels visualized by
831 coomassie blue staining. (D) Schematic representation of *Drosophila* Megator obtained from
832 the Eukaryotic Linear Motif (ELM) resource and Clustal Omega (EMBL-EBI) local sequence
833 alignment for the indicated Megator/Tpr orthologues. Amino acids in dark gray background
834 are conserved and amino acids in light gray background have similar chemical properties.
835 Symbols: * fully conserved residue; **:** conservation between groups of strongly similar
836 properties; **.** conservation between groups of weakly similar properties. Residues
837 phosphorylated by Mps1 were identified by mass spectrometry analysis after *in vitro* kinase
838 assay. Phospho-sites (P) were identified with MaxQuant/Andromeda with a decoy FDR of
839 0.01 on peptide and site level. (E) Pull-downs of recombinant purified MBP-Megator^{1187-}
840 $^{1655/WT}$, MBP-Megator$^{1187-1655/WT}$ phosphorylated by GST-Mps1, or MBP-Megator$^{1187-1655/T4D}$
841 by bead-immobilized 6xHis-Mad1$^{1-493}$ or 6xHis-BubR1$^{1-358}$ (negative control). Both beads
842 (B) and flow-through (FT) were blotted for the indicated proteins. (F) Quantification of
843 MBP-Megator binding to 6xHis-Mad1$^{1-493}$ from pull-downs in (E). The graph represents the
844 ratio between the chemiluminescence signal intensities of MBP-Megator and 6xHis-Mad1^{1-}
845 ^{493} from two independent experiments. The values obtained for MBP-Megator$^{1187-1655/WT}$ were
846 set to 1. (G,H) Representative immunofluorescence images (G) and schematic representation
847 (H) of EGFP-Megator$^{1187-1655}$ clustering by light-activated reversible inhibition by assembled
848 trap (LARIAT) in mitotic S2 cells. Fusion of CIB1 with the multimerization domain from
849 CaMKIIα (MP) forms dodecamers in the cytoplasm. The CRY2 photolyase homology region
850 (PHR) is fused with an anti-GFP nanobody that binds specifically to EGFP-Megator. Blue
851 light triggers CRY2 oligomerization and binding to CIB1, thus trapping EGFP-Megator into
852 multimeric protein clusters. In the dark, CRY2 reverts spontaneously to its ground state and
853 the clusters disassemble. LARIAT-induced clusters of EGFP-aPKC were used as negative
854 control. The insets display magnifications of the outlined regions. S2 cells were treated with
855 colchicine (30μM) for 10 hours and MG132 (20μM) for 4 hours followed by a 30 minute
856 period of blue light irradiation. Expression of LARIAT-modules, EGFP-Megator$^{1187-1655}$
857 transgenes and EGFP-aPKC was induced for 24 hours prior immunofluorescence analysis.
858 (I,J) Quantification of Mad1 levels at EGFP-Megator$^{1187-1655}$ clusters (I) and at kinetochores
859 (J). Mad1 fluorescence intensities at clusters were determined relative to GFP-Megator^{1187-}
860 ^{1655} signal (N≥114 clusters for each condition) and at kinetochores relative to Mad1 cytosolic
861 signal (N≥64 kinetochores for each condition). Data information: in (F), (I), and (J), data are
862 presented as mean ± SD. Asterisks indicate that differences between mean ranks are

bioRxiv preprint doi: https://doi.org/10.1101/659938; this version posted June 4, 2019. The copyright holder for this preprint (which was not certified by peer review) is the author/funder, who has granted bioRxiv a license to display the preprint in perpetuity. It is made available under aCC-BY-NC-ND 4.0 International license.

863 statistically significant, ** p<0.01, **** p<0.0001, (Kruskal-Wallis, Dunn´s multiple
864 comparison test). Scale bars: 5µm
865
866 **Figure 3: Recruitment of Mad1 to unattached kinetochores and robust SAC signaling**
867 **require phosphorylation of Megator by Mps1.** (A) Representative immunofluorescence
868 images of Mad1 localization in control and Megator-depleted interphase cells. The insets
869 display magnifications of the outlined regions. (B,C) Representative immunofluorescence
870 images (B) and corresponding quantifications (C) of Mad1 at the nuclear envelope of
871 interphase S2 cells depleted of endogenous Megator and expressing the indicated Megator-
872 EGFP transgenes. When indicated, cultures were incubated in the presence of Mps1 RNAi
873 for 120 hours. The insets display magnifications of the outlined regions. Mad1 fluorescence
874 intensities were determined relative to Megator-EGFP signal (N ≥ 41 cells for each
875 condition). (D,E) Representative immunofluorescence images (D) and corresponding
876 quantification (E) of Mad1 at unattached kinetochores of S2 cells depleted of endogenous
877 Megator and expressing the indicated Megator-EGFP transgenes. When indicated, cultures
878 were incubated in the presence of Mps1 RNAi for 120 hours. To generate unattached
879 kinetochores, cells were incubated with colchicine (30µM) and MG132 (20µM) for 30min
880 prior to fixation. The insets display magnifications of the outlined regions. Mad1
881 fluorescence intensities were determined relative to CID signal (N ≥ 125 kinetochores for
882 each condition). (F) Mitotic timings of S2 cells depleted of endogenous Megator and
883 expressing the indicated Megator-EGFP transgenes under unperturbed conditions or upon
884 addition of taxol (100nM) or colchicine (30µM) (N ≥ 11 cells for each condition). Expression
885 of Megator-EGFP transgenes in (B-F) was induced for 24 hours prior processing for
886 immunofluorescence analysis or live cell imaging. Data information: in (C) data is presented
887 as median with interquartile range; in (E) and (F) data is presented as mean ± SD. Asterisks
888 indicate that differences between mean ranks are statistically significant, * p<0.05, ** p<
889 0.01, *** p<0.001, **** p<0.0001 (Kruskal-Wallis, Dunn´s multiple comparison test in (C)
890 and (E) and Student's t-test in (F)). Scale bars: 5µm.
891
892 **Figure 4: Constitutively impaired Mad1-Megator interaction reduces C-Mad2 levels at**
893 **kinetochores and the strength of SAC signalling.** (A,B) Representative western blots (A)
894 and corresponding quantifications (B) of Megator, Mad1 and Mad2 protein levels in lysates
895 from control or Megator-depleted S2 cells expressing the indicated Megator-EGFP
896 transgenes. When indicated, cultures were incubated in the presence of Mps1 RNAi for 120h.

bioRxiv preprint doi: https://doi.org/10.1101/659938; this version posted June 4, 2019. The copyright holder for this preprint (which was not certified by peer review) is the author/funder, who has granted bioRxiv a license to display the preprint in perpetuity. It is made available under aCC-BY-NC-ND 4.0 International license.

897 The chemiluminescence signal intensities of Megator, Mad1 and Mad2 were determined
898 relative to tubulin signal. The graph represents the quantification of relative protein levels
899 from at least two independent experiments. The mean value obtained for control parental
900 cells was set to 1. (C,D) Representative immunofluorescence images (C) and corresponding
901 quantifications (D) of C-Mad2 at unattached kinetochores of S2 cells depleted of endogenous
902 Megator and expressing the indicated Megator-EGFP transgenes. When indicated, cultures
903 were incubated in the presence of Mps1 RNAi for 120 hours. To generate unattached
904 kinetochores, cells were incubated with colchicine (30µM) and MG132 (20µM) for 30min
905 prior to immunofluorescence analysis. The insets display magnifications of the outlined
906 regions. C-Mad2 fluorescence intensities were determined relative to CID signal ($N \geq 148$
907 kinetochores for each condition). (E) Mitotic timings of S2 cells depleted of endogenous
908 Megator and expressing the indicated Megator-EGFP transgenes under unperturbed
909 conditions or upon addition of taxol (100nM) or colchicine (30µM) ($N \geq 10$ cells for each
910 condition). Mitotic timings of S2 cells expressing Megator^{WT}-EGFP are the same as used in
911 Figure 3F. (F,G) Representative immunofluorescence images (F) and corresponding
912 quantifications (G) of C-Mad2 levels at unattached kinetochores of control or Megator-
913 depleted S2 cells treated with colchicine (30µM) and MG132 (20µM) for 30min. The insets
914 display magnifications of the outlined regions. C-Mad2 fluorescence intensities were
915 determined relative to CID signal ($N \geq 224$ kinetochores for each condition). (H) Mitotic
916 timings of control and Megator-depleted S2 cells under unperturbed conditions or upon
917 addition of taxol (100nM) or colchicine (30µM) ($N \geq 8$ cells for each condition). Expression
918 of Megator-EGFP transgenes in (A-E) was induced for 24 hours prior processing for
919 immunofluorescence analysis or live cell imaging. Data information: in (B) data is presented
920 as mean ± SEM; in (D), (E), (G), and (H), data are presented as mean ± SD. Asterisks
921 indicate that differences between mean ranks are statistically significant, *$p<0.05$, ** $p<0.01$,
922 ****$p<0.0001$, (Kruskal-Wallis, Dunn´s multiple comparison test in (D) and Student's t-test
923 in (E), (G) and (H). Scale bars: 5µm.

924

925 **Figure 5. Depletion of Megator restores Mad1 kinetochore recruitment and mitotic**
926 **fidelity in *Drosophila mps1-null* neuroblasts.** (A,B) Representative immunofluorescence
927 images with ploidy histograms (A) and corresponding quantifications (B) of Mad1 levels at
928 unattached kinetochores of w^{1118}, *InscGal4>UAS-MegatorRNAi*, ald^{G4422} or
929 ald^{G4422};*InscGal4>UAS-MegatorRNAi* neuroblasts treated with colchicine (50µM) for 1.5
930 hours. The insets display magnifications of the outlined regions. Mad1 fluorescence

bioRxiv preprint doi: https://doi.org/10.1101/659938; this version posted June 4, 2019. The copyright holder for this preprint (which was not certified by peer review) is the author/funder, who has granted bioRxiv a license to display the preprint in perpetuity. It is made available under aCC-BY-NC-ND 4.0 International license.

931 intensities were determined relative to Spc105 signal. (N≥91 kinetochores for each condition)
932 (C-E) Mitotic progression (C), mitotic timing (D) and percentage of anaphases with lagging
933 chromosomes (E) of w^{1118}, *InscGal4>UAS-MegatorRNAi*, ald^{G4422} or
934 ald^{G4422};*InscGal4>UAS-MegatorRNAi* neuroblasts co-expressing Jupiter-GFP and H2B-
935 mRFP. Mitotic progression was monitored through time-lapse microscopy and the mitotic
936 timing was defined as the time cells spent from nuclear envelope breakdown (NEB) to
937 anaphase onset (AO) (N ≥ 14 neuroblasts for each condition from at least two independent
938 experiments). The arrowhead in (C) points to a lagging chromosome. (F) Proposed model for
939 the control of Mad1 subcellular redistribution during the G2/M transition. In interphase,
940 inactive Mps1 (unphosphorylated T-loop) is retained in the cytoplasm and Mad1-C-Mad2
941 complexes are docked at the nucleoplasmic side of NPCs through Mad1 binding to Megator.
942 During prophase, active Mps1 (phosphorylated T-loop) becomes detectable in the nucleus
943 and is now able to phosphorylate Megator. This disrupts the nucleoporin interaction with
944 Mad1, hence ensuring timely release of Mad1-C-Mad2 from NPCs. Dissociation from
945 Megator enables Mad1-C-Mad2 to efficiently accumulate at prometaphase kinetochores and
946 instate robust SAC signalling. Data information: in (A), (B), (C), and (E), data are presented
947 as mean ± SD. Asterisks indicate that differences between mean ranks are statistically
948 significant, *p < 0.05, *** p<0.001, ****p<0.0001 (Kruskal-Wallis, Dunn's multiple
949 comparison test). Scale bars: 5µm.
950
951 **Figure S1: Additional information related to Figure 1.** (A) Kymograph representations of
952 Mad1-EFGP and Megator-EGFP localization pattern from movies in Figure 1A. (B) Data
953 corresponding to the quantifications of nuclear envelope Mad1-EFGP and Megator-EGFP
954 from Figure 1B plotted in the same graph for comparison purposes. (C) Representative
955 immunofluorescence images of EGFP-Mps1, $Mps1^{T490Ph}$ and Megator localization pattern in
956 interphase control S2 cells and interphase S2 cells expressing EGFP-$Mps1^{WT}$, EGFP-
957 $Mps1^{WT}$-NLS or EGFP-$Mps1^{KD}$-NLS. The insets display magnifications of the outlined
958 regions. Graphs represent the intensity profiles of GFP-Mps1, $Mps1^{T490Ph}$ and Megator signal
959 along the dotted lines. Scale bar: 5µm
960
961 **Figure S2. Kinetochore-extrinsic activity of Mps1 contributes for Mad1 kinetochore**
962 **recruitment** (A,B) Representative immunofluorescence images (A) and corresponding
963 quantifications (B) of Mad1 and Mps1 levels at unattached kinetochores of neuroblasts from
964 w^{1118} or ald^{G4422} flies. When indicated, EGFP-Mps1-C^{term} or EGFP-Mps1-WT transgenes

bioRxiv preprint doi: https://doi.org/10.1101/659938; this version posted June 4, 2019. The copyright holder for this preprint (which was not certified by peer review) is the author/funder, who has granted bioRxiv a license to display the preprint in perpetuity. It is made available under aCC-BY-NC-ND 4.0 International license.

965 were expressed under control of *Mps1* native promoter in an *ald*^{G4422} background. To
966 generate unattached kinetochores, neuroblasts were incubated with colchicine (50µM) for 1.5
967 hours. The insets display magnifications of the outlined regions. Mad1 and Mps1
968 fluorescence intensities were determined relative to Spc105 signal ($N \geq 106$ kinetochores for
969 each condition). (C) Western blot analysis of endogenous Mps1, EGFP-Mps1-WT and
970 EGFP-Mps1-C^{term} levels in total lysates of 3rd *instar* larval brains from (A). (D) Western blot
971 analysis of Mps1, Megator and Mad1 relative levels in control S2 cells and in cells depleted
972 of the indicated proteins. Cells were incubated with MG123 (20µM) for 1 hour and with
973 colchicine (30µM) for 2 hours. Asterisk denotes bands resulting from unspecific anti-GFP
974 blotting. (E, F) Representative immunofluorescence images (E) and corresponding
975 quantifications (F) of Mad1 and Mps1 levels at unattached kinetochores of control S2 cells
976 and cells depleted of the indicated proteins. Cells were incubated with MG123 (20µM) for 1
977 hour and with colchicine (30µM) for 2 hours. The insets display magnifications of the
978 outlined regions. Mad1 and Mps1 fluorescence intensities were determined relative to CID
979 signal ($N \geq 109$ kinetochore for Mad1, $N \geq 139$ kinetochores for Mps1). (G) Mitotic index
980 quantification based on H3^{Ser10Ph} staining of control S2 cells and cells depleted of the
981 indicated proteins. Cells were incubated with colchicine (30µM) for time periods indicated.
982 Data information: in (B), (F), and (G) data are presented as mean ± SD. Asterisks indicate
983 that differences between mean ranks are statistically significant, *$p<0.05$, ****$p<0.0001$
984 (Kruskal-Wallis, Dunn's multiple comparison test). Scale bars: 5µm.
985
986 **Figure S3: Depletion of Megator prevents intestinal dysplasia caused by lack of Mps1**
987 **activity in intestinal stem cells.** (A) Schematic representation of the *Drosophila* posterior
988 midgut epithelium under homeostatic conditions or after aneuploidy-induced dysplasia.
989 Aneuploid ISCs/EBs over-proliferate and accumulate causing epithelium dysplasia (Resende
990 et al., 2018). ISCs- intestinal stem cells, EBs – enteroblasts, EE –enteroendocrine cells, EC-
991 enterocytes BM - basement membrane, VM- visceral muscle. (B,C) Representative
992 immunofluorescence images (B) and corresponding quantifications (C) of the percentage of
993 ISCs/ EBs (GFP-positive) in intestines with ISCs/EBs depleted of the indicated proteins.
994 *GFP-UAS* was expressed alone or co-expressed with *UAS-MegatorRNAi* or *UAS-Mps1RNAi*
995 under control of the *EsgGAL4* promoter during the first 20 days of adult flies. The insets
996 display magnifications of the outlined regions. Quantification of percentage of ISCs/EBs
997 relative to total number of cells ($N \geq 40$ intestines). Data on graph represents mean ± SD.

bioRxiv preprint doi: https://doi.org/10.1101/659938; this version posted June 4, 2019. The copyright holder for this preprint (which was not certified by peer review) is the author/funder, who has granted bioRxiv a license to display the preprint in perpetuity. It is made available under aCC-BY-NC-ND 4.0 International license.

998 Asterisks indicate that differences between mean ranks are statistically significant, * p<0.05;
999 *** p<0.001 (Kruskal-Wallis, Dunn's multiple comparison test). Scale bar: 50µm.
1000
1001 **Figure S4: Timely phosphorylation of Megator coordinates Mad1 subcellular**
1002 **localization with cell cycle progression to ensure a fully-functional spindle assembly**
1003 **checkpoint.** Preventing Mps1-mediated phosphorylation of Megator on T1259, T1295,
1004 T1338 and T1390 (Megator^{T4A}) retains Mad1 associated with the nucleoporin during mitosis.
1005 This precludes proper recruitment of Mad1-C-Mad2 to prometaphase/unattached
1006 kinetochores and consequently compromises the strength of SAC signalling. On the other
1007 hand, constitutive phosphorylation of these residues (Megator^{T4D}) abrogates Mad1 interaction
1008 with Megator throughout the cell cycle. Though able to efficiently accumulate Mad1 at
1009 prometaphase/unattached kinetochores, Megator^{T4D} cells also exhibit a weakened SAC
1010 function. This likely results from reduced formation of Mad1-C-Mad2 heterotetramers at
1011 NPCs during interphase, which possibly limits the assembly of pre-mitotic MCC (Rodriguez-
1012 Bravo et al., 2014) and the association of C-Mad2 with kinetochores latter in mitosis. Hence,
1013 robust SAC function requires the interaction of Mad1 with Megator at NPCs to be tightly
1014 coordinated with cell cycle progression. Activation and nuclear import of Mps1 during late
1015 G2/prophase provides a molecular switch that ensures timely release of Mad1 from NPCs
1016 precisely when kinetochores must instate SAC signalling. This kinetochore-extrinsic
1017 mechanism enables the cell to produce MCC both at NPCs in interphase and at kinetochores
1018 during mitosis, so that the checkpoint is sufficiently robust to safeguard against chromosome
1019 mis-segregation.
1020
1021

bioRxiv preprint doi: https://doi.org/10.1101/659938; this version posted June 4, 2019. The copyright holder for this preprint (which was not certified by peer review) is the author/funder, who has granted bioRxiv a license to display the preprint in perpetuity. It is made available under aCC-BY-NC-ND 4.0 International license.

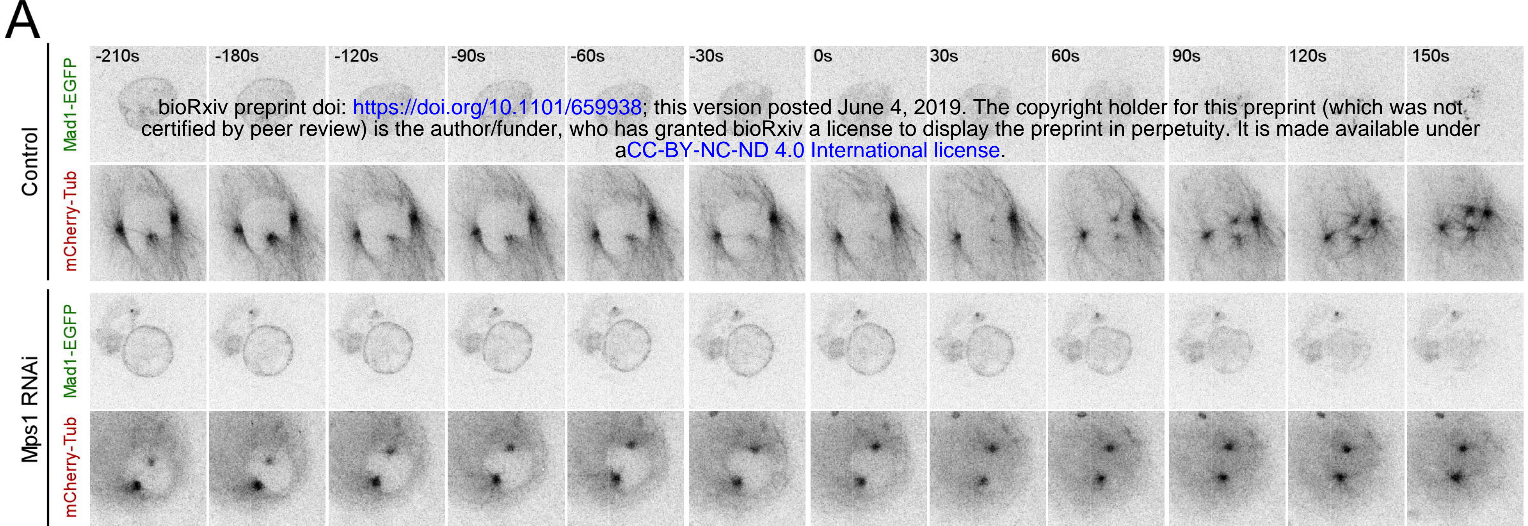

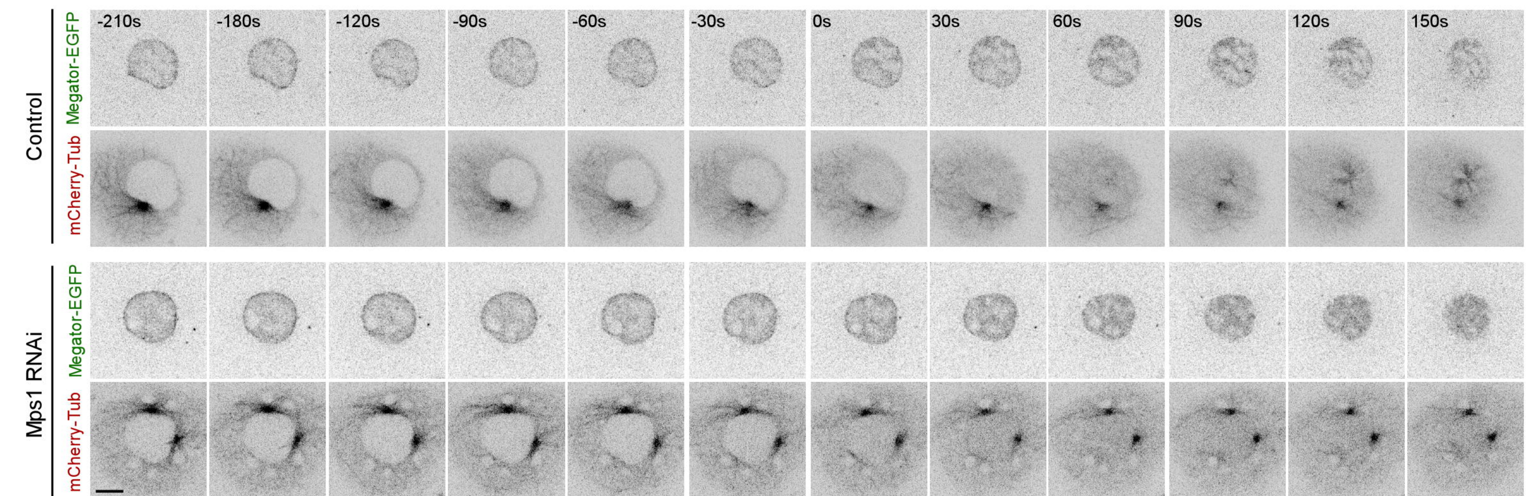

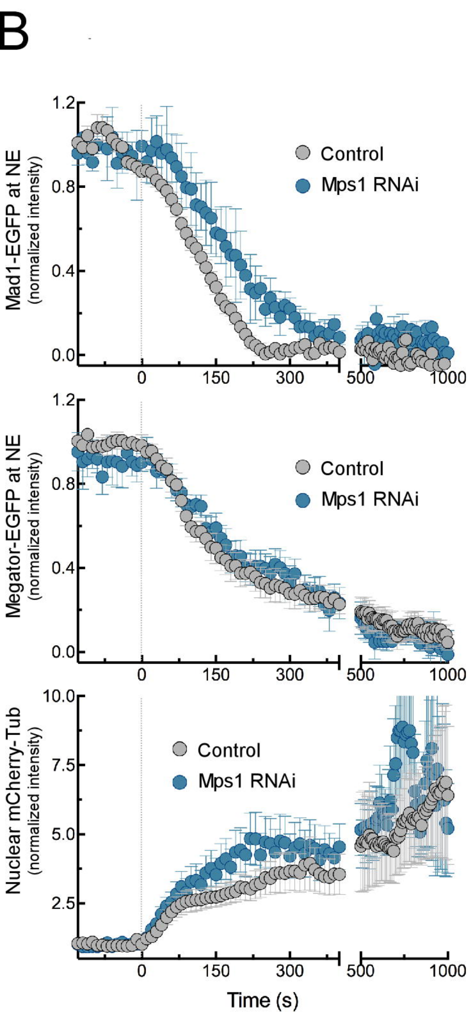

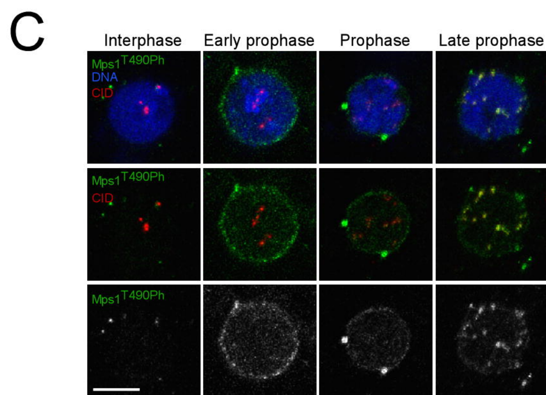

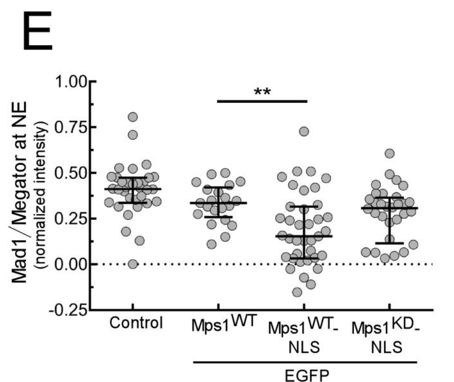

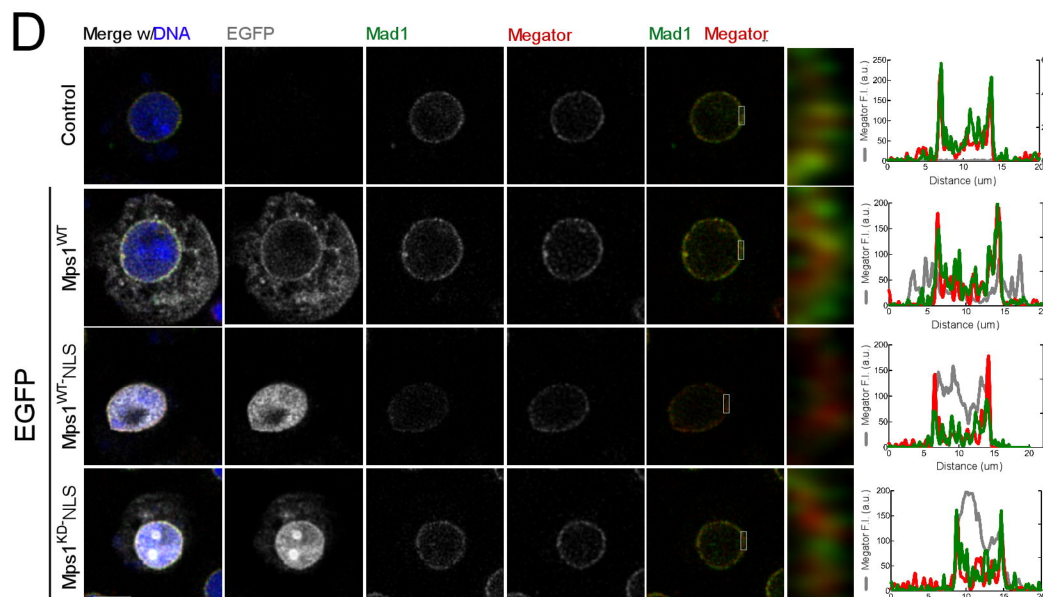

Osswald et al Figure 1

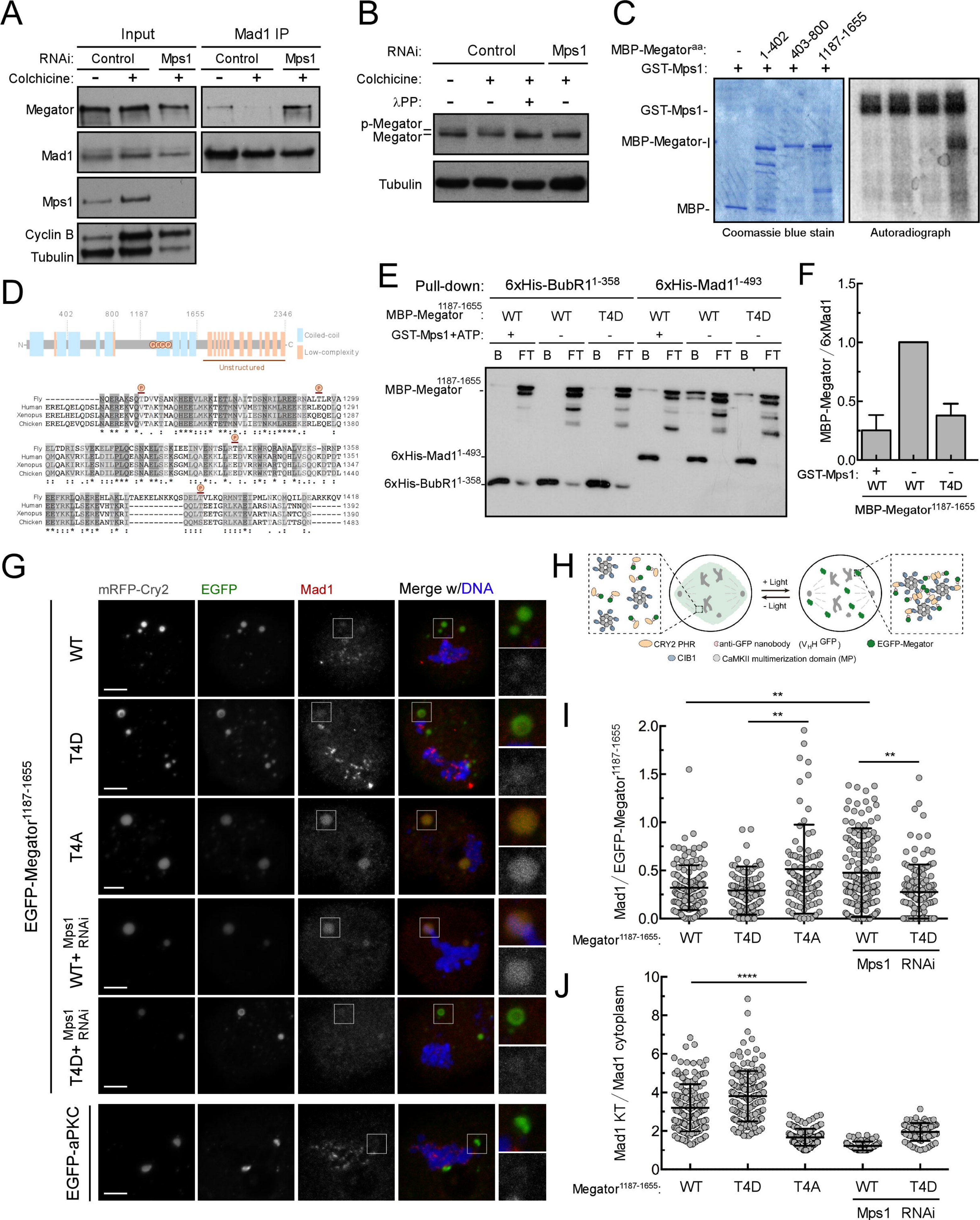

Osswald et al Figure 2

aCC-BY-ND 4.0 International license.

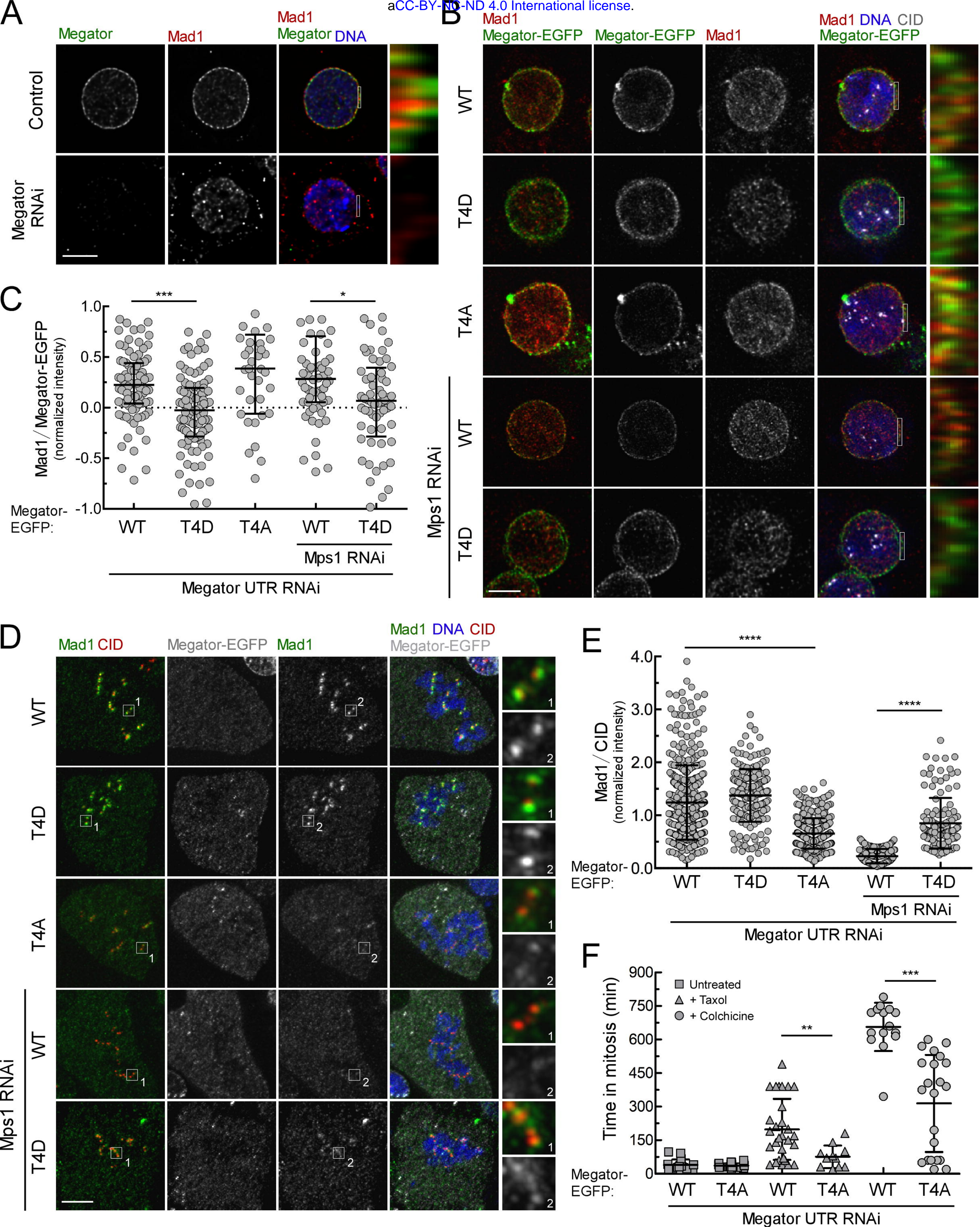

Osswald et al Figure 3

bioRxiv preprint doi: https://doi.org/10.1101/659938; this version posted June 4, 2019. The copyright holder for this preprint (which was not certified by peer review) is the author/funder, who has granted bioRxiv a license to display the preprint in perpetuity. It is made available under aCC-BY-NC-ND 4.0 International license.

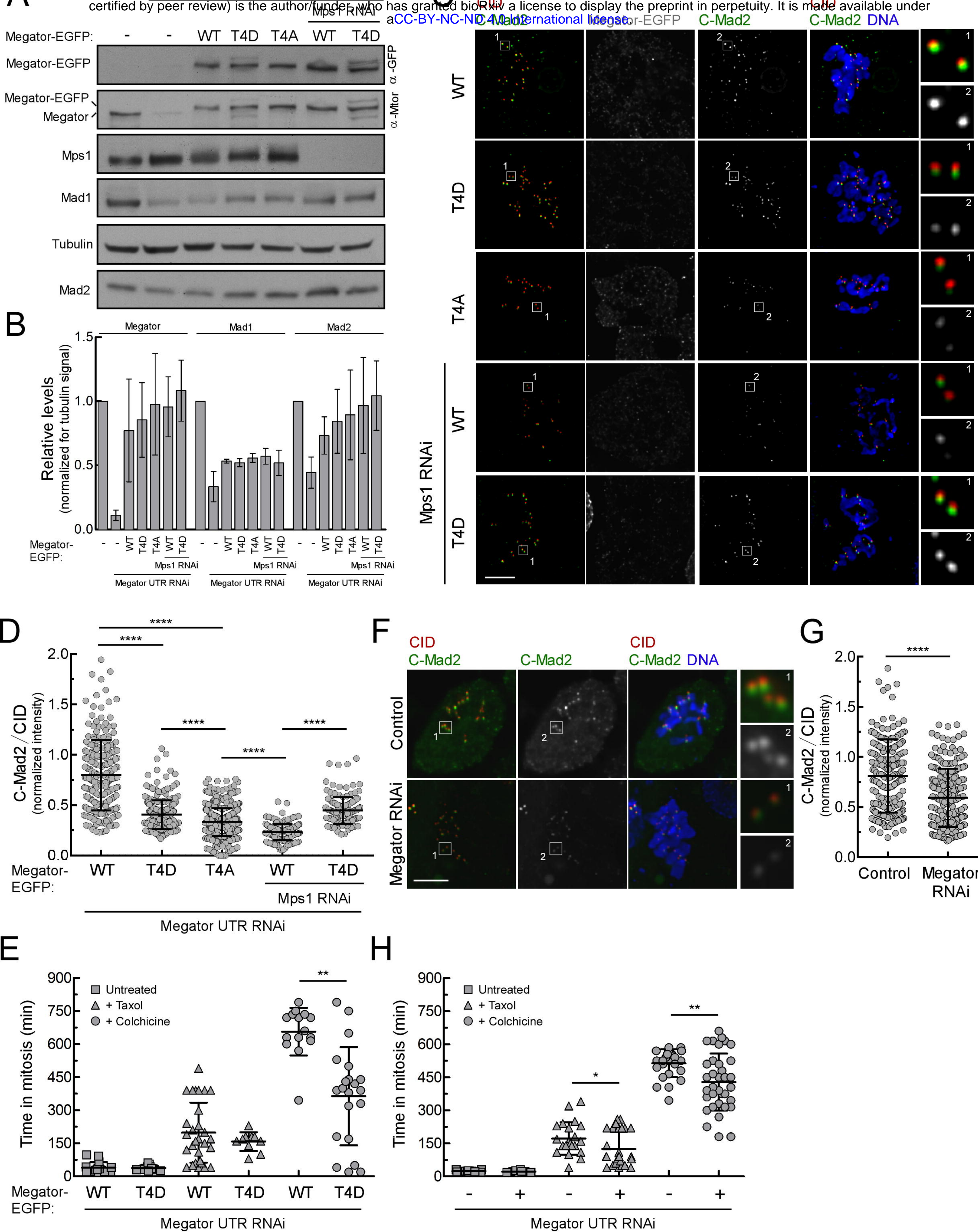

Osswald et al Figure 4

bioRxiv preprint doi: https://doi.org/10.1101/659938; this version posted June 4, 2019. The copyright holder for this preprint (which was not certified by peer review) is the author/funder, who has granted bioRxiv a license to display the preprint in perpetuity. It is made available under CC-BY-NC-ND 4.0 International license.

A

Spc105 Mad1 | Spc105 | Mad1 | Spc105 Mad1 DNA

w^{1118}

Megator RNAi

ald^{G4422}

ald^{G4422} Megator RNAi

% of neuroblasts

number of chromosomes

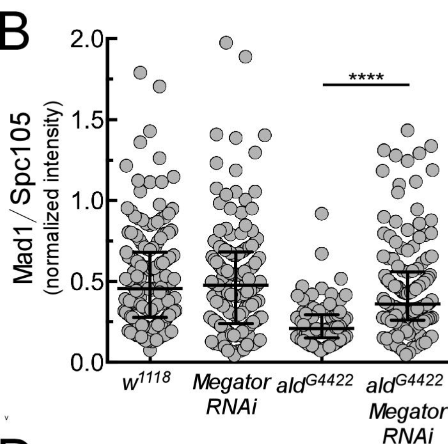

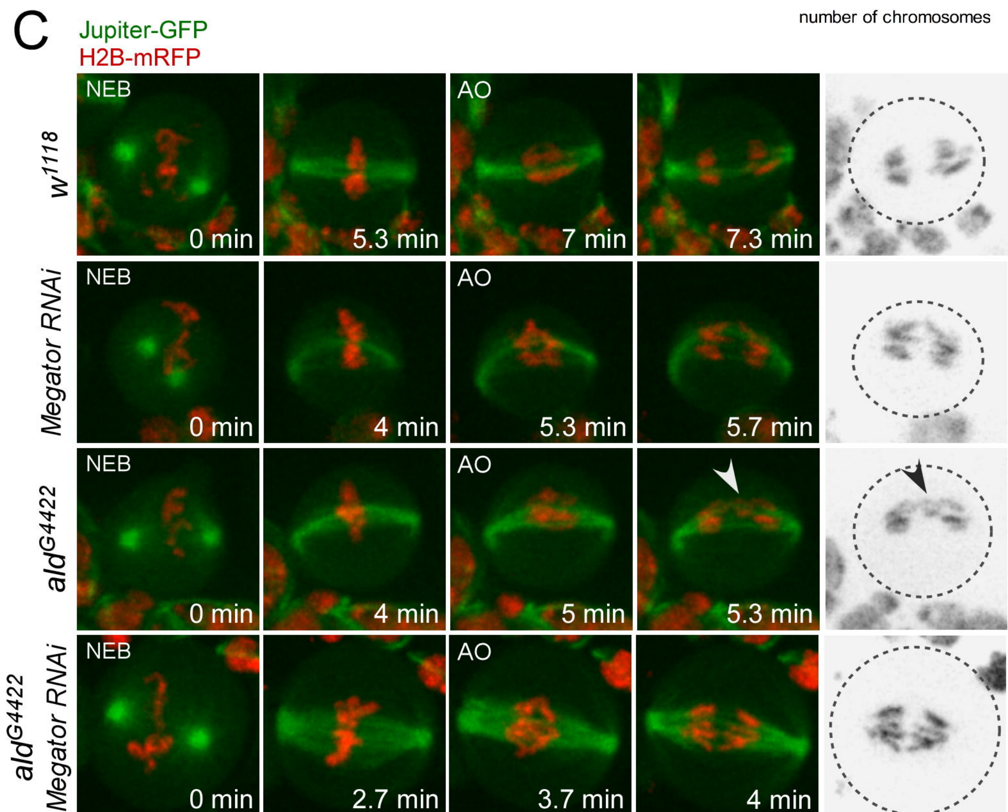

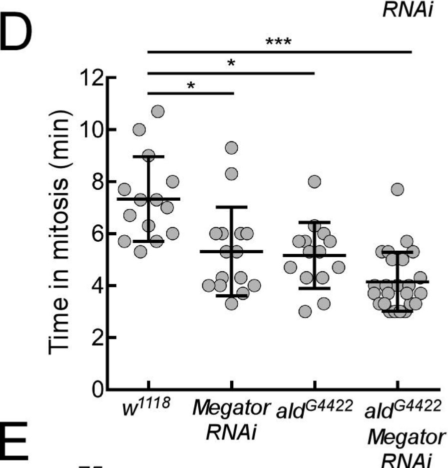

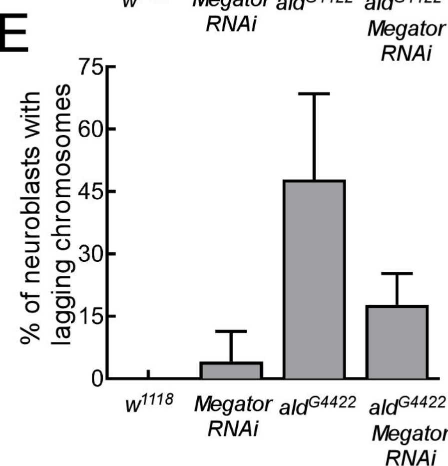

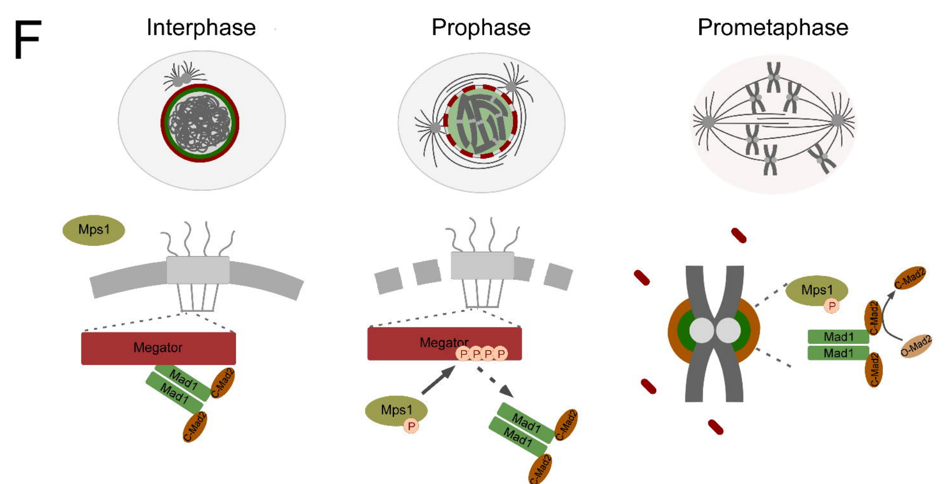

Osswald et al Figure 5

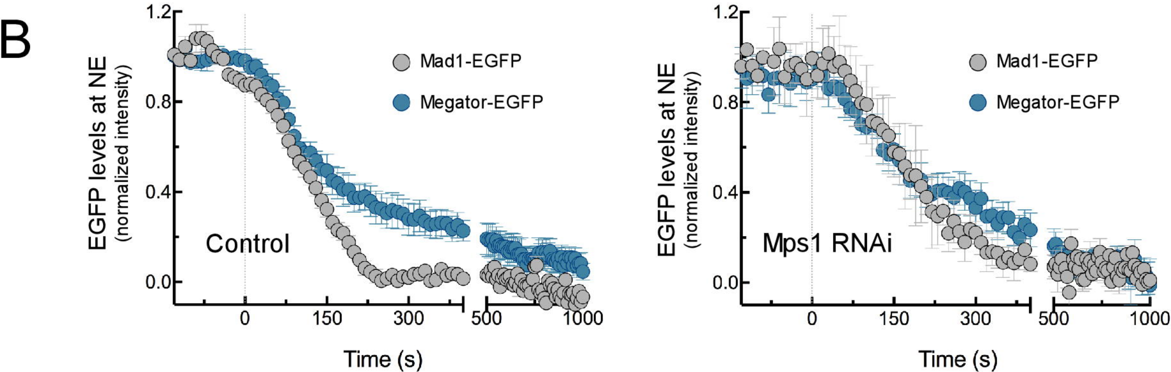

Osswald et al Figure S1

https://doi.org/10.1101/659938 ... copyright holder for this preprint (which was not ... the preprint in perpetuity. It is made available under CC-BY-NC-ND 4.0 International license.

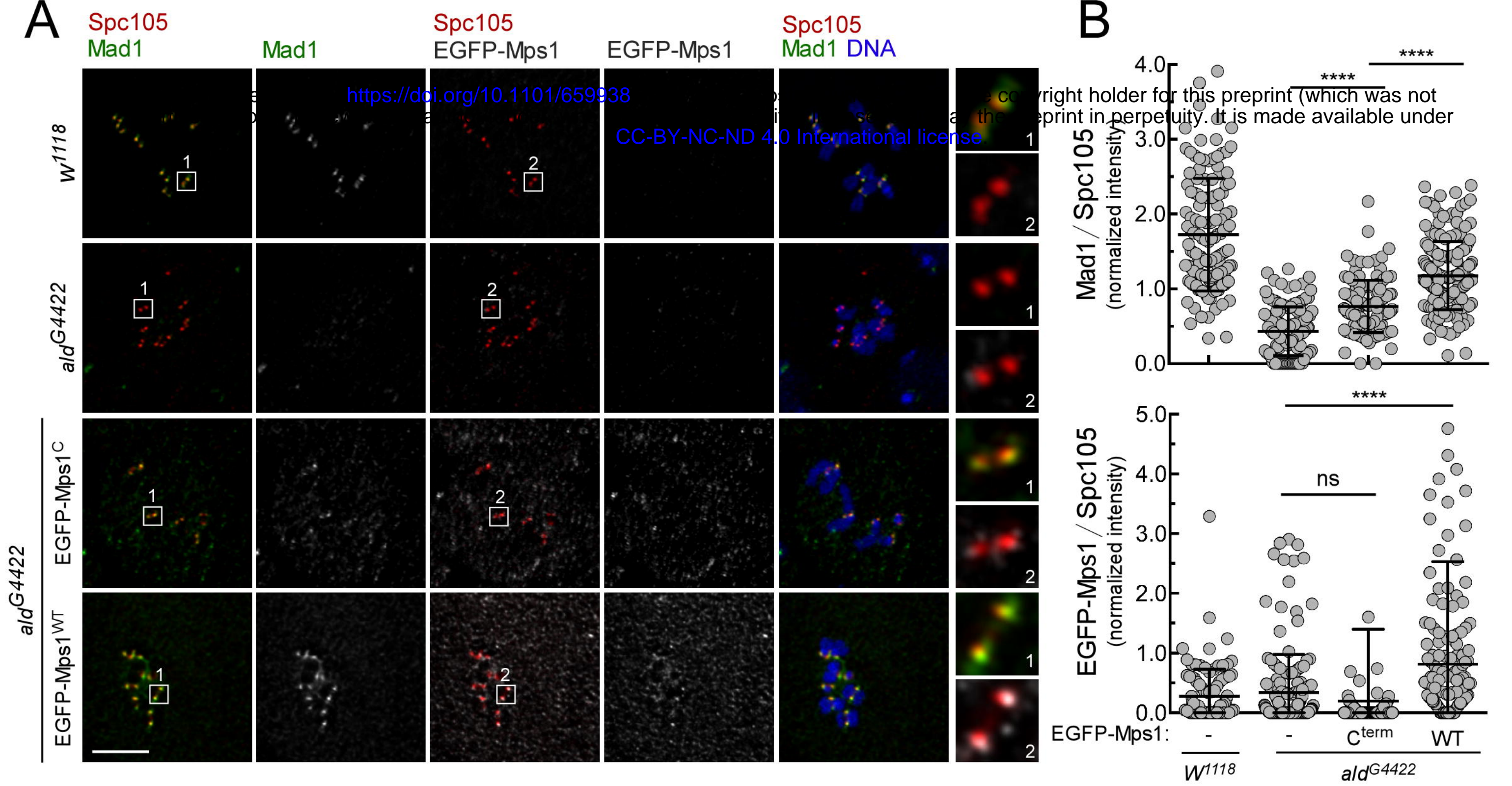

C
W^{1118} ald^{G4422}
EGFP-Mps1: - - C^{term} WT
EGFP-Mps1^{WT}
Mps1
α-Mps1
EGFP-Mps1^{WT}
*
α-GFP
EGFP-Mps1^{C}
Tubulin

D
RNAi: Control Mps1 Megator Mps1+ Megator
Megator
Mps1
Mad1
Tubulin

E
CID Mad1
Mad1
CID Mps1
Mps1
CID Mad1 Mps1 DNA
Control
Megator RNAi
Mps1 RNAi
Mps1+ Megator RNAi

F
Mad1 / CID (normalized intensity)
Mps1 / CID (normalized intensity)
****
****
****
RNAi: Control Megator Mps1 Mps1 Megator
Control Megator Mps1 Mps1 Megator

G
% Mitotic cells
*
ns
Time in colch (h): 0 6 12 24 0 6 12 24 0 6 12 24 0 6 12 24
RNAi: Control Mps1 Megator Mps1+ Megator

Osswald et al Figure S2

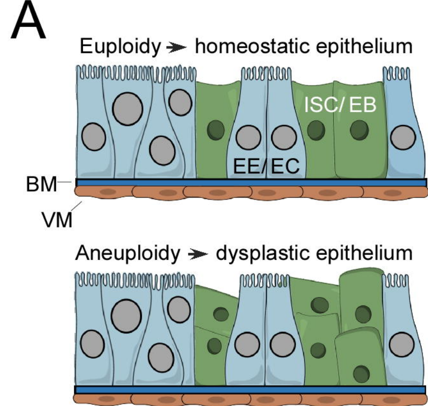

B

DNA
GFP (ISCs/EBs)
Merge
Control
Mps1 RNAi
Mps1+
Megator RNAi

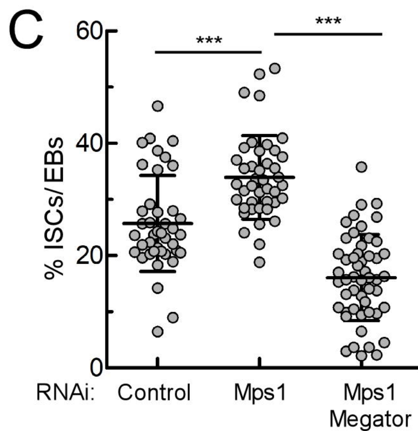

Osswald et al Figure S3

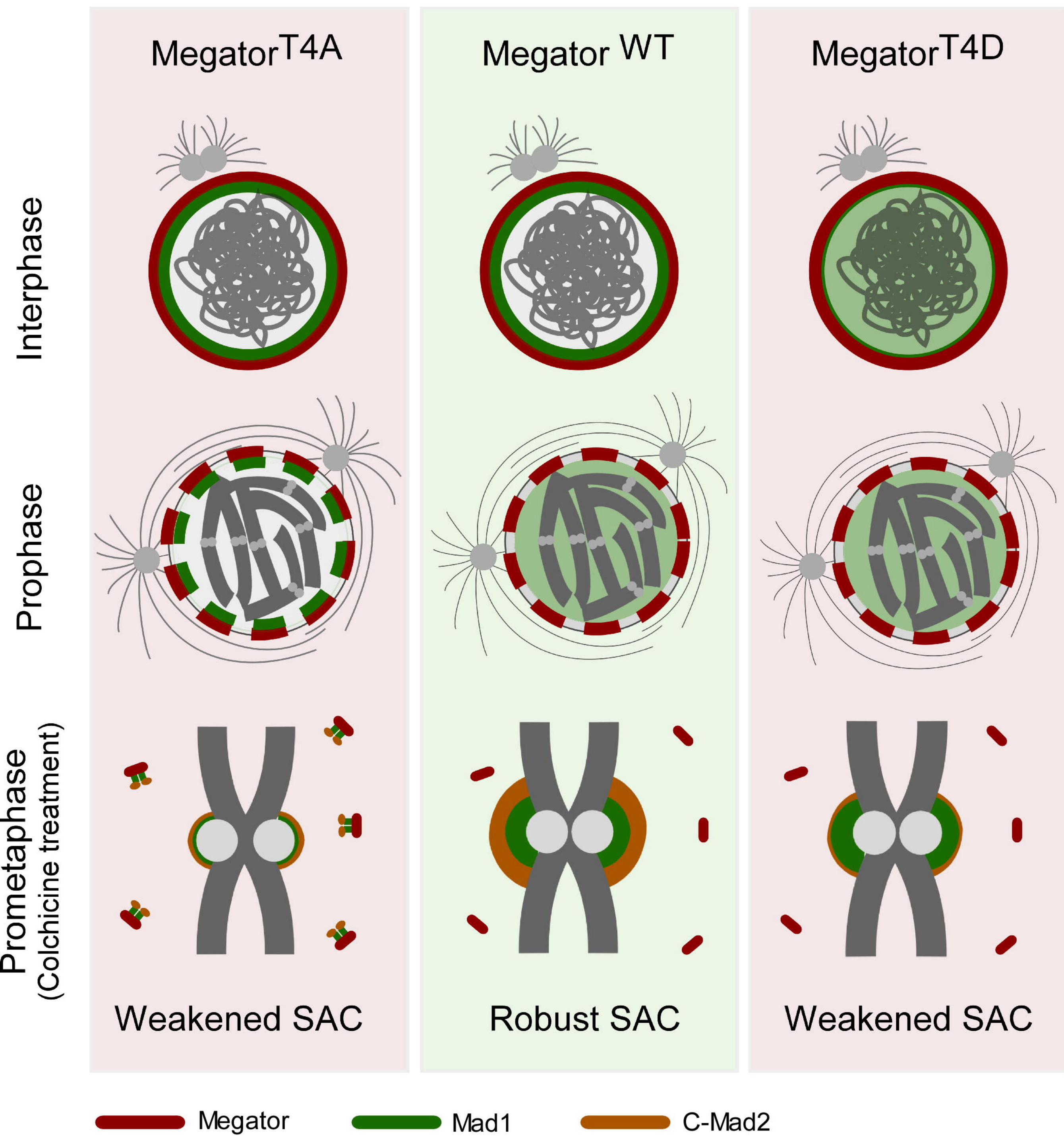

Osswald et al Figure S4